Mark Joseph Lattery
118 Words

Fully Leptonic Decays of B Mesons

The CLEO-II detector at the Cornell Electron Storage Ring (CESR) has been used to study the world's largest sample of B-meson decays. Using this sample we have searched for two classes of fully-leptonic B decays: the purely leptonic decays $B \to \ell\overline{\nu}_\ell$ ($\ell = e, \mu, \tau$) and the radiative leptonic decays $B \to \ell\overline{\nu}_\ell\gamma$ ($\ell = e, \mu$). Observations of these decay modes will allow us to test and define the standard model of electroweak interactions. For the decays $B \to e\overline{\nu}_e$, $B \to \mu\overline{\nu}_\mu$, and $B \to \tau\overline{\nu}_\tau$ we obtain branching fraction upper limits of 1.3×10^{-5}, 1.1×10^{-5}, and 2.2×10^{-3} at the 90% confidence level, respectively. For the decays $B \to e\overline{\nu}_e\gamma$ and $B \to \mu\overline{\nu}_\mu\gamma$, we obtain branching fraction upper limits of 2.0×10^{-4} and 5.2×10^{-5} at the 90% confidence level, respectively.

UNIVERSITY OF MINNESOTA

This is to certify that I have examined this bound copy of a doctoral thesis by

Mark Joseph Lattery

and have found that it is complete and satisfactory in all respects and that any and all revisions required by the final examining committee have been made.

Professor Yuichi Kubota

(Faculty Adviser)

GRADUATE SCHOOL

Fully Leptonic Decays of B Mesons

A THESIS
SUBMITTED TO THE FACULTY OF THE GRADUATE SCHOOL
OF THE UNIVERSITY OF MINNESOTA
BY

Mark Joseph Lattery

IN PARTIAL FULFILLMENT OF THE REQUIREMENTS
FOR THE DEGREE OF
DOCTOR OF PHILOSOPHY

July, 1996

Fully Leptonic Decays of B Mesons

by Mark Joseph Lattery

Under the supervision of Professor Yuichi Kubota

ABSTRACT

The CLEO-II detector at the Cornell Electron Storage Ring (CESR) has been used to study the world's largest sample of B-meson decays. Using this sample we have searched for two classes of fully-leptonic B decays: the purely leptonic decays $B \to \ell\overline{\nu}_\ell$ ($\ell = e, \mu, \tau$) and the radiative leptonic decays $B \to \ell\overline{\nu}_\ell\gamma$ ($\ell = e, \mu$). Observations of these decay modes will allow us to test and define the standard model of electroweak interactions. For the decays $B \to e\overline{\nu}_e$, $B \to \mu\overline{\nu}_\mu$, and $B \to \tau\overline{\nu}_\tau$ we obtain branching fraction upper limits of 1.3×10^{-5}, 1.1×10^{-5}, and 2.2×10^{-3} at the 90% confidence level, respectively. For the decays $B \to e\overline{\nu}_e\gamma$ and $B \to \mu\overline{\nu}_\mu\gamma$, we obtain branching fraction upper limits of 2.0×10^{-4} and 5.2×10^{-5} at the 90% confidence level, respectively.

Acknowledgements

I would like to thank my wife, Stephanie, for the endless nights she waited up for me. No person has contributed more to the success of my graduate education than her. Her love is of a rare, perserving sort. I would also like to thank my mother who always loves me and, in spite of life's many struggles, always seems to fight her way through. To all my brothers and sisters who were born into or married into the Lattery family, I thank you for your support and humor. To the Doty family, I thank you for your love, acceptance, and belief in me.

I would also like to thank the many high school teachers, undergraduate professors, and graduate professors that contributed to my love for physics: Mr. Trenda, Dr. Richard Fuller, Dr. Thomas Greenlee, Dr. Richard Peterson, Dr. Dave Cinabro, and Dr. Ritchie Patterson. I would also like to thank my thesis advisor, Dr. Yuichi Kubota, for his kindness and guidance.

This work could not have been completed without the effort of approximately 200 students and professors within the CLEO Collaboration. In particular, I would like to thank Dr. Jeff Nelson for his willingness to help me, and many others.

Finally, I would like to thank God. He loved me, He helped me, He answered my prayers, He forgave me, He forgave me some more, and finally, He helped me to finish. Through His son, Jesus, He gave me a life worth living...

Dedication

To my lovely wife, Stephanie

Table of Contents

"Run straight to the goal,

with purpose in every step."

– I Corinthians 9:27

"If you're not failing a lot,

you are probably not being as creative as you could be."

– B. Douglas

Chapter 1

Particles and Interactions

1.1 Introduction

A belief exists among physicists that a fundamental simplicity underlies the observed diversity of the Universe. This belief has guided mankind on a scientific journey to seek out, understand, and finally unify the particles and forces of nature. We now believe that nature contrives an enormous complexity of structure and dynamics from just six leptons and six quarks (and their antimatter counterparts). Four interactions exist between these particles: electromagnetism, gravity and the strong and weak forces. In the subatomic realm, interactions between particles can produce changes in energy and momentum, and even transitions between particles; an interaction can also affect a particle in isolation, in a spontaneous decay process.

The world we normally experience is composed almost entirely of one lepton, the electron, and two kinds of quarks, labelled "up" and "down" (or, simply u and d). Quarks can be bound together in groups of three, called baryons, or in groups of two, called mesons; baryons and mesons form a larger class of particles called hadrons. In a simplified picture, the proton consists of two up quarks and a down quark ($p = uud$), and the neutron consists of two down quarks and an up quark ($n = udd$).

The electron, up, and down quarks have less well known anti-matter counterparts: the positron (e^+), the anti-up quark $\bar{u}$, and the anti-down quark $\bar{d}$. Anti-particles have the same mass as their corresponding particles, but carry the opposite charge. Anti-particles may also be found within hadrons. For example, the positively charged pi-meson (or simply, pion) consists of an up quark and an anti-down quark ($\pi^+ = u\bar{d}$).

In addition to the u and d quarks, two other pairs of quarks exist: strange (s) and charm (c), and beauty (b) and truth (t). The subject of this thesis is the charged B meson, consisting of either an anti-beauty quark and an up quark ($B^+ = \bar{b}u$), or a beauty quark and an anti-up quark ($B^- = b\bar{u}$).

1.2 Particles

Modern relativistic field theory succeeded in providing a theoretical framework within which we can describe quantitatively physical phenomenon involving the creation and annihilation of particles. This theory has been greatly successful in predicting a wide variety of scattering and decay processes. Within field theory, the fields are quantized and particles emerge as quanta of their associated fields. Particles with half-integral spin ($1/2\hbar$, $3/2\hbar$,...) are called *fermions*, while those with integral-spin (0, $1\hbar$, $2\hbar$,...) are called *bosons*. Fermions can be divided into two additional categories: leptons and quarks.

Leptons naturally fall into three doublets, or families, as shown in Table 1.1. The electron is much lighter ($m_e = 0.5110\,\mathrm{MeV/c^2}$),[1] than the muon ($m_\mu = 105.7\,\mathrm{MeV/c^2}$) or tau ($m_\tau = 1777.1\,\mathrm{MeV/c^2}$) [1] [2]. Each of these leptons is associated with a neutral partner called a neutrino ($m_\nu \approx 0\,\mathrm{MeV/c^2}$) [3]. Quarks also fall into three families. While the up, down and strange quarks (u, d and s) are known to be very light (a few to

[1] An MeV is a million eV, the energy an electron, or other singly charged particle, gains in traversing a voltage difference of one Volt. Similarly, a GeV is a billion eV. Masses are usually measured in $\mathrm{MeV/c^2}$, meaning that if the mass is M, the rest energy is Mc^2 MeV.

a few hundred MeV/c^2), the charm, beauty and truth quarks (c, b and t) are heavy, with $m_c \approx (1.3-1.5)$ GeV/c^2, $m_b \approx (4.7-5.0)$ GeV/c^2, and $m_t \approx (160-192)$ GeV/c^2 [4] [17]. Using scattering experiments, leptons and quarks are known to be many orders of magnitude smaller (10^{-18} m) than the size of atoms (10^{-10} m) [5].

It is experimentally observed that heavier leptons and quarks decay to lighter ones via the weak force. While these transitions usually observe family lines, they occasionally cross them. In particular, the beauty quark may decay to the lighter c quark or u quark. The relative rate of such decays provides an opportunity to test and define the current theory of particle interactions, the standard model.

Table 1.1: Fermions and their Electric Charges.

$$\begin{array}{lcccc} \text{leptons} & \begin{pmatrix} e \\ \nu_e \end{pmatrix} & \begin{pmatrix} \mu \\ \nu_\mu \end{pmatrix} & \begin{pmatrix} \tau \\ \nu_\tau \end{pmatrix} & \begin{array}{c} e \\ 0 \end{array} \\ \\ \text{quarks} & \begin{pmatrix} u \\ d \end{pmatrix} & \begin{pmatrix} c \\ s \end{pmatrix} & \begin{pmatrix} t \\ b \end{pmatrix} & \begin{array}{c} +\frac{2}{3}e \\ -\frac{1}{3}e \end{array} \end{array}$$

Table 1.2: Fundamental Interactions of the Standard Model

Force	Boson	Symbol	Charge	Spin	Mass (GeV/c^2)
Strong	gluon	g	0	1	0
Electromagnetic	photon	γ	0	1	0
Weak	W	$W^\pm$	$\pm e$	1	81
	Z	Z^0	0	1	92

In this thesis, we ask the question: how often does a charged B meson collapse through a mutual annihilation of its constituent quarks and fully materialize into leptons? As we discuss in the next chapter, the answer to this question is dependent on the frequency of $b \rightarrow u$ transitions.

1.3 Interactions

According to the standard model, three fundamental interactions occur between the fermions. These interactions are carried by the bosons listed in Table 1.2. The electromagnetic interaction is mediated by photons, and may couple to any of the charged leptons and quarks. The weak interaction is mediated by the very heavy $W^{\pm}$ and Z^0 bosons, and may couple to quarks and leptons of the same or different family of fermions. The strong interaction is mediated by massless gluons, and may couple to any two quarks.[2]

1.3.1 Gauge Theories

The dynamics of interacting fermions are defined by a Lagrangian density [6]. In the standard model, each Lagrangian density is generated by requiring local gauge invariance. Physically this means that tranformations of the form

$$\psi(\vec{x}, t) \rightarrow e^{iH(\vec{x},t)}\psi(\vec{x}, t) \tag{1.1}$$

will not produce physically observable effects. The quantity $H(\vec{x}, t)$ is referred to as the gauge, and may be any $n \times n$ Hermitian matrix.

The theory of the electromagnetic interaction, quantum electrodynamics (QED), is constructed by applying the principle of local gauge invariance to the free Dirac Lagrangian. In this case the gauge H is just a real number, and the corresponding operator $U = e^{iH}$ belongs to the group U(1). To construct a locally invariant Lagrangian, it is necessary to introduce a vector field, A_μ. This field contains the gauge freedom necessary to absorb changes in the Lagrangian produced by a local gauge tranformation. The desired symmetry is achieved only if the vector field is long-range and massless.

[2]The gravitational interaction, not considered a part of the standard model, is believed to be carried by gravitons, and may couple to any two particles with mass.

The resulting QED interaction Lagrangian can be written:

$$\mathcal{L}_{QED} = (e\bar{\psi}\gamma^{\mu}\psi)A_{\mu}, \tag{1.2}$$

where e is the electric charge, γ are the Dirac matrices related to the spin of the fermions, and the quantity in parentheses is the fermion current. The resulting field equations are precisely those predicted by classical electrodynamics. Here, the fermions are quanta of the Dirac fields, $\bar{\psi}$, and photons are quanta of the electrodynamic field, A_{μ}.

The theory of strong interactions, quantum chromodynamics (QCD), arises from the special unitary symmetry SU(3). The procedure for constructing the QCD Lagrangian is completely analogous to the procedure used in QED. In this case, however, the gauge H is a 3×3 matrix, and the corresponding operator U is a unitary matrix with determinant 1. The three dimensions correspond to the three color "charges" of quarks: red, green, and blue. The interaction Lagrangian describing the "color" force between a quark q_{α} of color α and quark q_{β} of color β is given by:

$$\mathcal{L}_{QCD} = g_3 \sum \bar{q_{\alpha}}\gamma^{\mu}\lambda^{\delta}_{\alpha\beta}q_{\beta}G^{\delta}_{\mu}, \tag{1.3}$$

where G is the chromoelectric field, g_3 is the coupling strength, and γ and λ are the Dirac and Gell-Mann matrices related to the spin of the quarks and color of the gluons, respectively. The chromoelectric field produces changes in the quark colors, and the color difference is carried away by the gluons. The gluon involved in the coupling of q_{α} and q_{β} will carry away colors α and β. From three colors, eight independent gluon combinations can be constructed. Because gluons carry color, they may strongly interact with each other. There is good evidence that this complicated set of interactions is responsible for *quark confinement*, the phenomenon that prevents quarks from existing in isolation [7]. In addition, the dynamics of the chromoelectric field are known to produce an "antiscreening effect" called asymtotic freedom which leads to a progressively weaker force between quarks as they approach one another (or equivalently, as the momentum involved in an interaction increases).

The electromagnetic and the weak interactions have been integrated into a single gauge theory based on a $\mathrm{SU(2)_L} \times \mathrm{U(1)}$ symmetry. In the electroweak theory, the interaction Lagrangian for the first family or "generation" of fermion is:

$$\begin{aligned}
\mathcal{L}_{EW} &= \sum_{f=l,q} g_1(\bar{f}\gamma^\mu f)A^\mu \\
&+ \frac{g_2}{\cos\theta_W} \sum_{f=l,q} \left[\bar{f}_L\gamma^\mu f_L(T_f^3 - Q_f \sin^2\theta_W) + \bar{f}_R\gamma^\mu f_R(-Q_f \sin^2\theta_W)\right] Z_\mu \\
&+ \frac{g_2}{\sqrt{2}} \left[(\bar{u_L}\gamma^\mu d_L + \bar{\nu_e}_L\gamma^\mu e_L)W_\mu^+ + (\text{Hermitian Conjugate})\right], \qquad (1.4)
\end{aligned}$$

where f and $\bar{f}$ are the fields of the fermions, A is the field of the photon, and Z and W are the fields of the two weak gauge bosons; g_1 is the electric coupling strength (or electric charge), g_2 is the weak coupling strength, and T_f^3 is the third component of weak isospin of the interacting fermions. The subscripts L and R denote the chirality, or handedness, of the fermions. For massless fermions, the chirality is equal to the helicity, which is positive (negative) if the fermion spin is directed toward (away from) its direction of motion. The Weinberg or weak mixing angle, θ_W, is a measure of the relative strength of the electromagnetic coupling and weak coupling strength. At energies below 100 GeV, $\sin^2\theta_W \approx 0.23$. In electroweak interactions, the neutral currents involve left- and right-handed fermions, while charge currents involve *only* left-handed fermions. An important consequence of the left-handed charged current is parity violation, the hallmark of the weak interaction.

All electoweak processes can be represented by Feynman diagrams. As an example, the coupling of a charged-W boson to a lepton and neutrino is shown in Figure 1.1.[3] This coupling can occur a number of different ways. In the first diagram, a lepton emits a W and becomes a neutrino; in the second diagram, a W produces a charged lepton

[3] In this thesis, the time coordinate of a Feynman diagram flows horizontally.

and neutrino; and, in the third diagram, a charged lepton and neutrino annihilate to produce a W. The photon and Z boson couple to neutral currents in a similar manner.

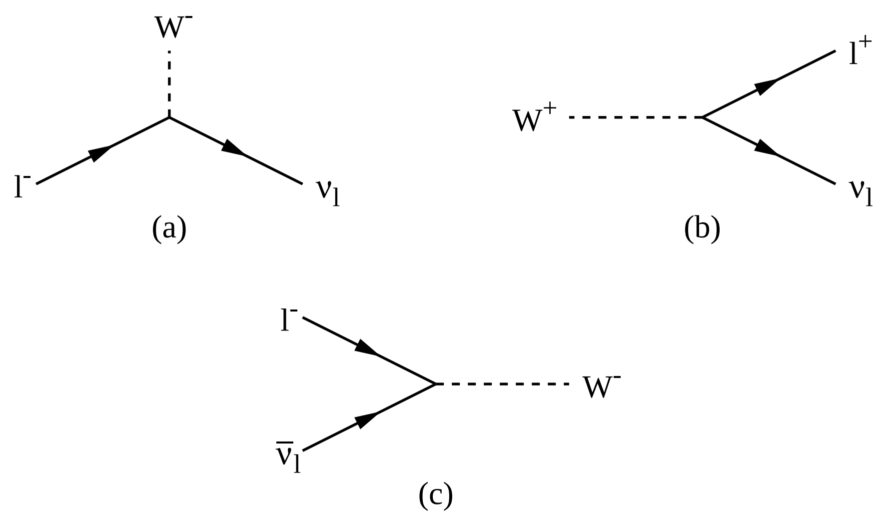

Figure 1.1: The basic interactions involving a W boson. (a) A lepton emits a W and becomes a different lepton. (b) A W produces a charged and a neutral lepton. (c) A charged lepton and neutral lepton annihilate to produce a W.

1.3.2 The Higgs Mechanism and the CKM Matrix

The electroweak theory as described above is known to be flawed. The gauge symmetry $SU(2)_L \times U(1)$ is invariant only if the fermions and bosons are massless. To remedy the situation, it is assumed that the underlying gauge symmetry is *spontaneously* broken. The symmetry breaking mechanism must not only generate the fermion and boson masses, but also lead to a renormalizable theory. In the Weinberg-Salam (WS) model, this is accomplished by introducing a doublet of complex Higgs fields, expanding the Higgs fields around an asymmetrical ground state, and demanding local gauge invariance.

The fermions in the WS model acquire mass through their couplings to the Higgs field. The terms representing the fermion-Higgs interaction in the Lagrangian are not necessarily diagonal in fermion generations [8]. Since fermion-Higgs interaction must be expressed in terms mass eigenstates, the weak eigenstates giving currents diagonal in generations are not the same as the mass eigenstates. Hence, integenerational mixing between fermion can occur.

To express the fermion-Higgs interaction in terms of mass eigenstates, the mass matrix is diagonalized using a pair of unitary transformations (one for each quark charge) relating the physical and weak quark bases. The product of unitary matrices that accomplishes this task, and which appears in the charge-current interaction Lagrangian, is known as the *mixing matrix*. For neutral currents the mass matrix stays diagonal and mixing does not occur [9].

The mixing matrix is unitary by construction, and therefore contains n^2 parameters. However, an arbitrary choice of phases for the quark fields can be used to eliminate 2n parameters. An overall phase can be chosen to render one of these operations ineffective, so we can remove a total of $2n-1$ phases. Of the n^2-2n+1 parameters, it can be shown that $\frac{1}{2}n(n-1)$ are real parameters and $\frac{1}{2}(n-1)(n-2)$ are imaginary parameters [10].

For two generations ($n = 2$), the mixing matrix contains one real parameter: the Cabibbo angle, θ_{C}. The resulting charge current (CC) part of the Lagrangian is:

$$\mathcal{L}_{\mathrm{CC}} = W_+^{\mu}(\bar{u}_L\bar{c}_L)\gamma_\mu \begin{pmatrix} \cos\theta_{\mathrm{C}} & \sin\theta_{\mathrm{C}} \\ -\sin\theta_{\mathrm{C}} & \cos\theta_{\mathrm{C}} \end{pmatrix} \begin{pmatrix} d_L \\ s_L \end{pmatrix} + h.c. \tag{1.5}$$

where all coupling constants are real. The well-known GIM mechanism uses the notion of "Cabibbo-rotated" quark states to explain the suppression of flavor-changing neutral currents, and justify the existence of the charm quark.

For three generations ($n = 3$), the resulting charge current part of the Lagrangian is:

$$\mathcal{L}_{\mathrm{CC}} = W_+^{\mu}(\bar{u}_L \bar{c}_L \bar{t}_L)\gamma_\mu \begin{pmatrix} V_{ud} & V_{us} & V_{ub} \\ V_{cd} & V_{cs} & V_{cb} \\ V_{td} & V_{ts} & V_{tb} \end{pmatrix} \begin{pmatrix} d_L \\ s_L \\ b_L \end{pmatrix} + h.c. \tag{1.6}$$

The mixing matrix for three generations is referred to as the Cabbibo-Kabayashi-Maskawa (CKM) matrix. Like fermion masses, the CKM matrix elements are fundamental input parameters, and must be determined experimentally. For three generations, the CKM matrix contains four independent quantities: three real parameters (or angles), and one imaginary parameter (a complex phase). The presence of a complex phase in the CKM matrix is believed to be responsible for CP violation in charged-current interactions.

1.3.3 Measuring the CKM Matrix

Experimentally, cross-generational mixing is known to be small. Guided by this observation, a useful expression for the CKM matrix may be obtained by expanding the matrix in the small parameter $\lambda = \sin\theta_{\mathrm{C}} \approx 0.22$ [11], where θ_{C} is the Cabibbo angle. This parameterization was first given by Wolfenstein [12], and is written as:

$$\mathbf{V} = \begin{pmatrix} 1 - \frac{1}{2}\lambda^2 & \lambda & A\lambda^3(\rho - i\eta) \\ -\lambda & 1 - \frac{1}{2}\lambda^2 & A\lambda^2 \\ A\lambda^3(1-\rho-i\eta) & -A\lambda^2 & 1 \end{pmatrix}. \tag{1.7}$$

As shown in this parametrization, the diagonal elements V_{ud}, V_{cs}, V_{tb} are close to unity (0.97-1.00), and the off-diagonal elements are much smaller in magnitude. That is, weak interactions nearly respect the quark generations, but not completely. The relative strength of the charged current couplings for leptons and quarks is represented in Figure 1.2. As an example, the rate for the process $B \to \pi\ell\nu$, which involves a $b \to u$ transition, is suppressed by a factor $|V_{ub}|^2 = 9.0 \times 10^{-6}$, and is therefore rarely observed.

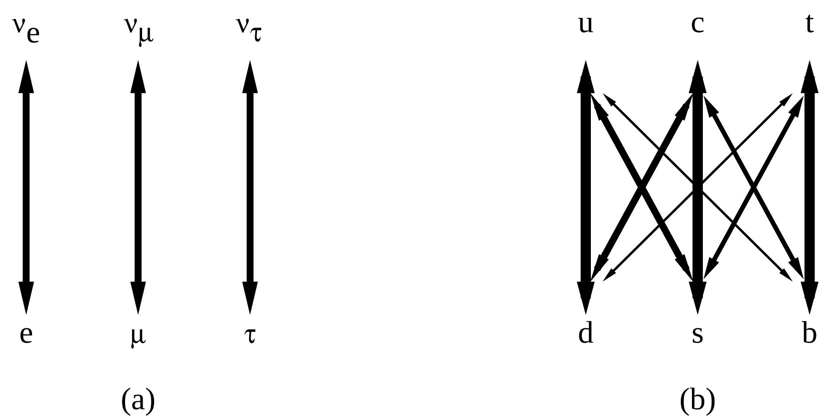

Figure 1.2: The possible charged current couplings for (a) leptons and (b) quarks. In (b), the strongest transitions correspond to the boldest lines.

Currently, only A and λ have been well measured with $A \approx 0.94 \pm 0.10$ and $\lambda = 0.2196 \pm 0.0023$. However, rough estimates of ρ and η can be obtained by measuring the b-quark couplings of W-mediated B decays. The Feynman diagrams for several types of B decays is given in Figure 1.3 and Figure 1.4. In this thesis, we will examine the probability that a B meson decays by the annihilation diagram (Figure 1.4(c)). In Chapter 2, we discuss how an observation of this decay would constrain the experimental values of ρ and η.

The Unitarity Relation

One important test of the the standard model is obtained by experimentally verifying the unitarity of the CKM matrix. The unitarity condition can be expressed as:

$$V_{ud}V_{ub}{}^{*} + V_{cd}V_{cb}{}^{*} + V_{td}V_{tb}{}^{*} = 0 \tag{1.8}$$

In terms of the Wolfenstein parameters, this condition defines the "unitarity triangle" in the complex (ρ,η) plane (see Figure 1.5). Using the approximation $V_{ud}{\approx}V_{td}{\approx}1$, the upper

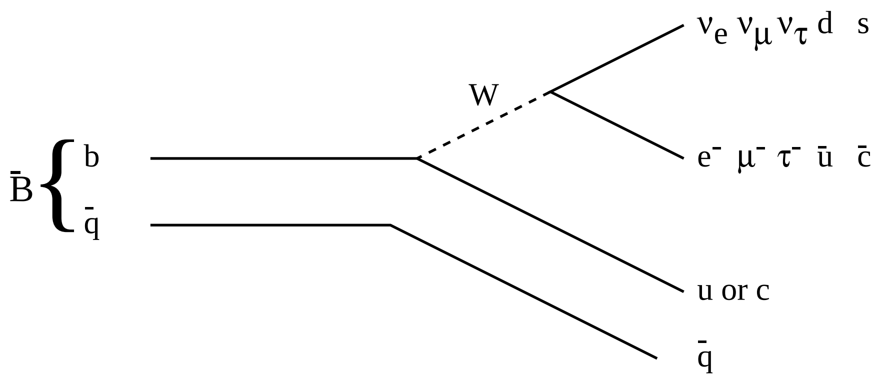

Figure 1.3: The spectator decay of a $\overline{B}$ meson.

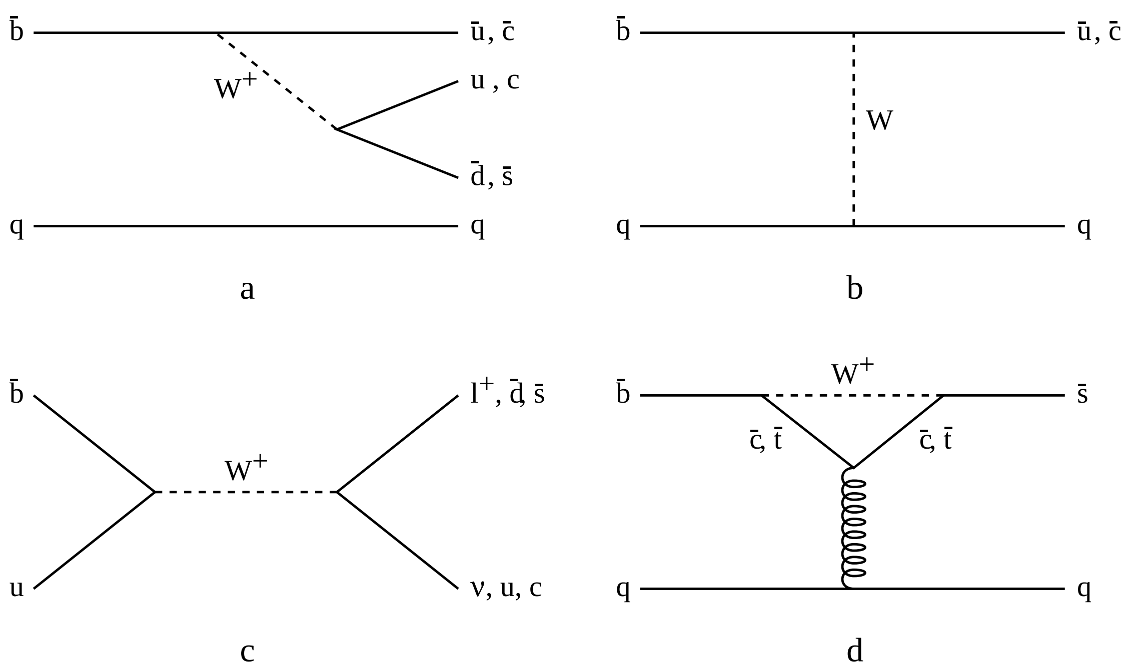

Figure 1.4: Other types of B meson decay. They are called (a) color mixed, (b) exchange, (c) annihilation, and (d) penguin decays.

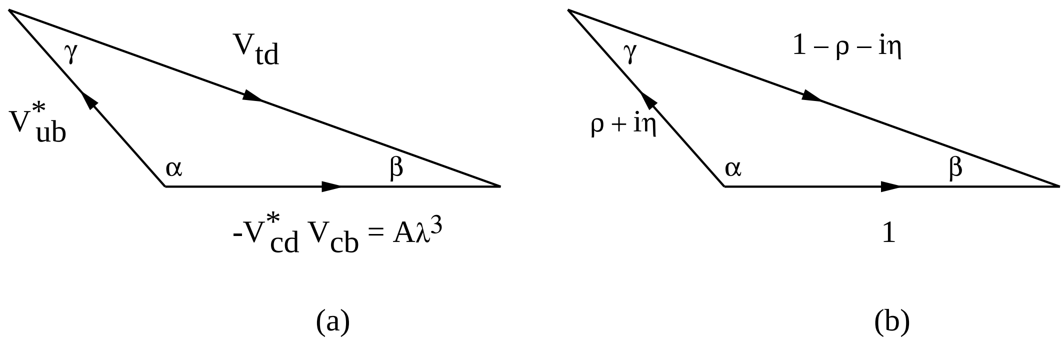

Figure 1.5: The unitarity triangle (a) in terms of the CKM matrix elements and (b) in terms of the Wolfenstein parameters.

two sides of the triangle may be normalized to $V_{ub}{}^*/(A\lambda^3) = \rho + i\eta$ and $V_{td}/(A\lambda^3) = 1-\rho-i\eta$. The unitarity condition requires that the observed values of the CKM matrix elements close the triangle.

The Existence of CP Violation

Since time-reversal (T) invariance demands $V = V^*$, the presence of the imaginary phase η in the CKM matrix implies the existence of T-violating processes in the weak interaction [13]. The existence of T-violation also implies a joint charge-conjugation plus parity (CP) violation, since it is impossible to violate CPT invariance without drastically altering the structure of quantum field theory [14].

The existence of CP violation has been confirmed in the neutral kaon sector where a small rate asymmetry (10^{-2}) is observed between $K_{\mathrm{L}}^0 \to \ell^- \overline{\nu}_\ell \pi^+$ and its CP-conjugate decay, $K_{\mathrm{L}}^0 \to \ell^+ \nu_\ell \pi^-$. However, the prediction of CP violation in neutral B decays has yet to be confirmed, and its observation stands as an important test of the standard model. A clear understanding of CP violation may also hold the key to understanding the dominance of matter over antimatter in the universe.

1.3.4 The Status of the Standard Model

The standard model has proven to be extremely effective in predicting physical phenomenon. To date, no significant discrepancies have been found between the standard model and experimental observation. However, the standard model is incomplete. The model does not account for the pattern of quark and lepton masses or the values of the CKM matrix elements. In all, it contains twenty or more theoretical parameters: the coupling strengths of the strong, weak, and electromagnetic interactions, the masses of the quarks and leptons, the mass of the Higgs boson, and the parameters specifying the interactions. By the criterion of simplicity set out at the beginning of this chapter, the standard model is lacking. However, a critical examination of the standard model may eventually lead to more powerful theories.

To test the standard model, and theories beyond the standard model, it is necessary to study particle interactions at higher and higher energies ($>$ 1 TeV). Of immediate importance is the need to confirm the existence of the Higgs boson, and thereby confirm the Higgs mechanism as an explanation of spontaneous symmetry breaking in the electroweak interaction. Currently, the Large Hadron Collider (LHC) being constructed at the European particle physics laboratory (CERN) is designed to do this. In addition, the nature of CP violation must be better understood. The B factories under construction at the Stanford Linear Accelerator Center (SLAC), and at the Japanese laboratory KEK, as well as the upgrade of the Cornell Electron Storage Ring (CESR), may facilitate this understanding.

Ultimately, the goal of theoretical and experimental efforts in elementary particle physics is to provide a unified understanding of all interactions of nature. Conspicuously missing from our discussion is the gravitational interaction. Whether gravity can be described in a quantum theory and unified with other forces remains another open question. Evidence exists at higher energies that the coupling strengths of the gravitational, electromagnetic, weak, and strong interactions converge at extremely high energies (10^{15} GeV). This convergence may indicate a single fundamental symmetry underlying all interactions. Examples of theories that attempt to specify this symmetry are string theory and supersymmetry; however, these theories have been subjected to little experimental scrutiny.

Chapter 2

Fully Leptonic Decays

The measurement of f_B and f_B^*, the leptonic decay constants of the B and B^* mesons, represents one of the main goals of the current and future experimental investigations in heavy quark physics [16]. *P. Colangelo*

2.1 Theoretical Motivation

One of the primary objectives of current experimental particle physics is to determine the values of all nine CKM matrix elements. As mentioned in Chapter 1, this objective can be reduced to the measurement of four independent parameters, which in the Wolfenstein parameterization are A, λ, ρ, and η. While the values of A and λ are well-established, ρ and η are currently poorly known. To evaluate these parameters current experimental efforts have relied on measurements of the CKM mixing angles V_{ub} and V_{cb}, from inclusive semileptonic B decays, and the $B^0\overline{B}^0$ mixing parameter, x_d. The functional dependence of these measurements on η and ρ is given by:

$$|\frac{V_{ub}}{V_{cb}}| \propto (\rho^2 + \eta^2)^{\frac{1}{2}}, \quad \text{and} \tag{2.1}$$

$$(\frac{\Delta M}{\Gamma}) \propto ((1-\rho)^2 + \eta^2) f_B^2. \tag{2.2}$$

Unfortunately, the constraint from $B^0\overline{B}^0$ mixing depends on the poorly known quantity f_B, the B decay constant, which describes how often two quarks overlap inside a B meson. The B decay constant has not been measured; theoretical estimates vary from near the pion decay constant of 130 MeV by QCD sum rules [18] to around 370 MeV by lattice QCD calculations in the static quark limit [19]. Given a precision measurement of f_B, a solution for ρ and η is obtained from the interesection of two circles, defined by Equations 2.1 and 2.2, in the $\rho - \eta$ plane (see Figure 2.1).

The only direct experimental means to access f_B is through an observation of purely leptonic decays $B \to \ell\overline{\nu}_\ell$.[1] An alternative, albeit model-dependent, means to access f_B is also provided through an observation of the radiative leptonic decays $B \to \ell\overline{\nu}_\ell + \gamma$. We refer to $B \to \ell\overline{\nu}_\ell$ and its radiative partner $B \to \ell\overline{\nu}_\ell + \gamma$ collectively as fully leptonic B decays. The goal of this thesis is to observe such decays and measure f_B. An unexpectedly large rate for these decays would have major implications for the standard model.

2.2 $B \to \ell\bar{\nu}_\ell$: The Annihilation Diagram

Purely leptonic B-meson decays proceed through the annihilation diagram in complete analogy to pion decays. The Feynman diagram for this decay is given in Figure 2.2(a). The constituent quarks of the B meson annihilate via the weak interaction to form a virtual W boson. After propagating a short distance, the W produces one of three lepton pairs: $e\overline{\nu}_e$, $\mu\overline{\nu}_\mu$, or $\tau\overline{\nu}_\tau$. The branching fraction for this process is given by:

---

[1] Throughout this thesis decays of the type $B \to \ell\bar{\nu}_\ell X$ refer to both $B^- \to \ell^-\bar{\nu}_\ell X$ and $B^+ \to \ell^+\nu_\ell X$, where $\ell = e, \mu, or \tau$.

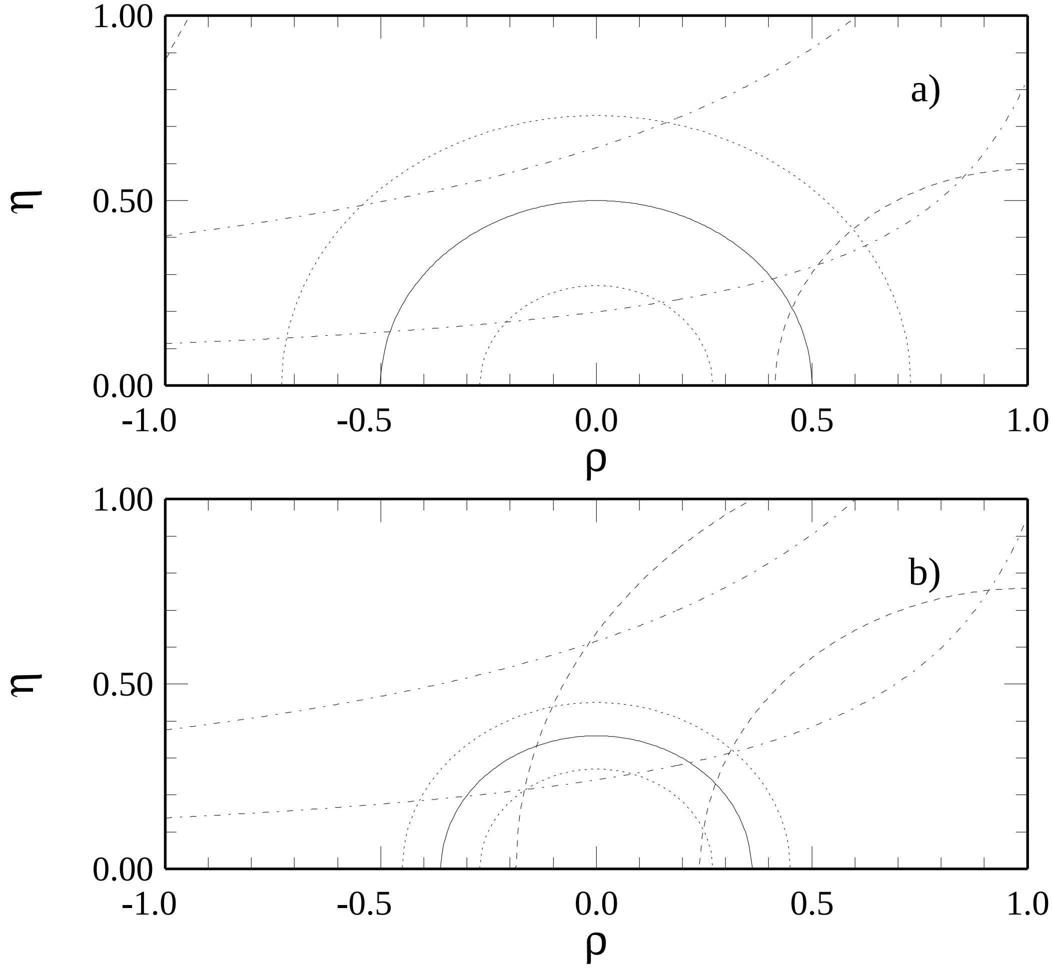

Figure 2.1: Constraints on the Wolfenstein parameters ρ and η. The constraint from $|V_{ub}/V_{cb}|$ is shown as a solid line (the central value) and a dotted line (1 standard deviation). The constraint from $B^0\overline{B}^0$ mixing by dashed lines and the constraints from CP-violating K_L^0 decays is shown by dot-dashed lines. (a) The constraints obtained from 1992 CLEO II measurement is compared with (b) the 1994 CLEO II measurement. (Courtesy of Jeff Nelson of the CLEO Collaboration.)

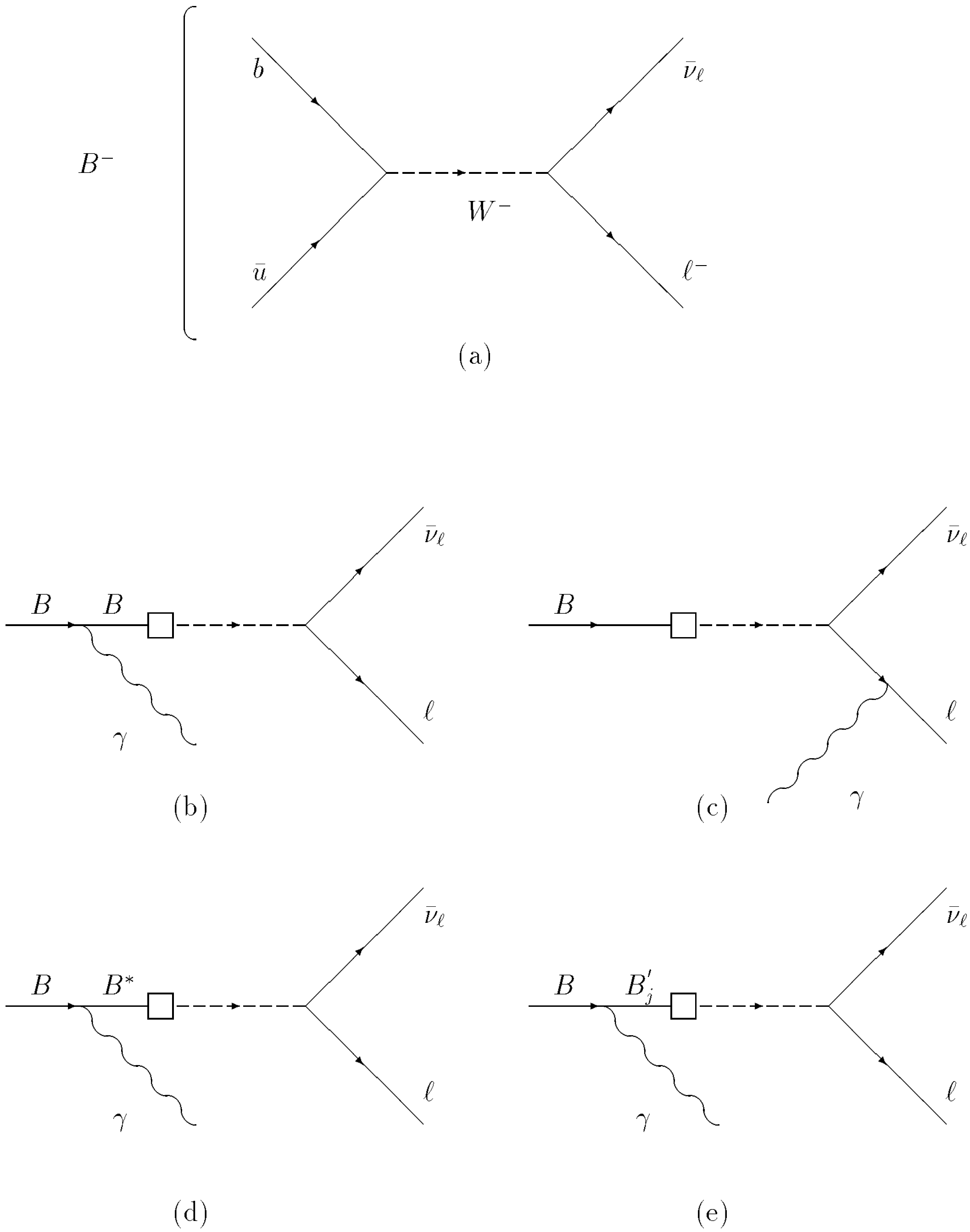

Figure 2.2: Feynman Diagrams for Fully Leptonic B Decays: (a) annihilation diagram, (b) Internal Bremmstrahlung diagram (initial-state radiation), (c) Internal Bremmstrahlung diagram (final-state radiation), (d) Structure Dependent diagram involving a vector meson (B^*) in the intermediate state, and (e) Structure Dependent diagram involving an axial-vector meson ($B^{'}$) in the intermediate state.

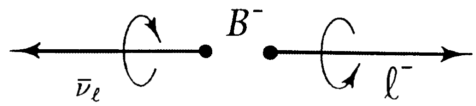

Figure 2.3: Helicity States in $B \to \ell\overline{\nu}_\ell$ Decay

$$\mathcal{B}(B \to \ell\overline{\nu}_\ell) = \frac{G_F^2 m_B m_\ell^2}{8\pi}\left(1 - \frac{m_\ell^2}{m_B^2}\right)^2 f_B^2 |V_{ub}|^2 \tau_B, \tag{2.3}$$

where G_F is the Fermi coupling constant, m_B and m_ℓ are the B-meson and lepton masses, τ_B is the charged-B lifetime, and V_{ub} is the CKM mixing angle for $b{\to}u$ transitions. The remaining factor is f_B, the B-meson decay constant, which for non-relativistic models defines the light quark wave function at the origin (the location of the b quark). All quantities in this decay rate are well established except for f_B and V_{ub}. The factor V_{ub} has been measured through a study of inclusive charmless semileptonic decays [20], and is currently known to 25−30%. Hence, the parameter f_B can be determined through an experimental observation of $B \to \ell\overline{\nu}_\ell$ decays.

The experimental difficulty in measuring $B \to \ell\overline{\nu}_\ell$ is due primarily to the well-known effect of helicity suppression which lowers its rate. To understand this effect, consider the decay $B^- \to \ell\overline{\nu}_\ell$ in the B rest frame (Figure 2.3), where $\ell = e$. Since the B has zero spin, the electron and neutrino must have the same helicity by angular momentum conservation. Since the weak interaction produces exclusively right-handed $\overline{\nu}_e$s, both the neutrino and electron must have helicity $H = +1$. However, since electrons produced by weak interaction are preferentially left-handed, the amplitude for this process is suppressed. The dependence of helicity suppression on the lepton mass is given by:

$$\text{Helicity Suppression} \;\propto\; 1 - \beta_l = \frac{2m_l^2}{m_B^2 + m_l^2}, \tag{2.4}$$

where β_l is the velocity of the lepton. The helicity suppression factor for τ, μ and e is approximately 1/5, 1/1000, and 1/50,000,000, respectively. The experimental confirmation of helicity suppression in $\pi^- \to \ell^- \overline{\nu}_\ell$ decays [21] is one of the great achievements of the standard model. The estimated branching fractions for purely leptonic B decays are:

$$\begin{aligned} \mathcal{B}(B^- \to \tau^- \overline{\nu}_\tau) &= 5.5 \times 10^{-5}, && (2.5) \\ \mathcal{B}(B^- \to \mu^- \overline{\nu}_\mu) &= 2.5 \times 10^{-7}, \quad \text{and} && (2.6) \\ \mathcal{B}(B^- \to e^- \overline{\nu}_e) &= 5.8 \times 10^{-12}, && (2.7) \\ & && (2.8) \end{aligned}$$

where we use $\tau_{\mathrm{B}} = 1.6$ ps, $f_B = 190\,\mathrm{MeV}$, and $V_{ub} = 0.003$, as reasonable values for these parameters [22] [23] [24].

According to CPT invariance, we expect the branching fractions for $B^- \to \ell^- \overline{\nu}_\ell$ and $B^+ \to \ell^+ \nu_\ell$ to be identical. The relatively large $B \to \tau \overline{\nu}_\tau$ decay rate suggests that it is the least difficult channel to study experimentally. However, other experimental factors related to decay dynamics make searches for $B \to \mu \overline{\nu}_\mu$ and $B \to \tau \overline{\nu}_\tau$ comparable in difficulty. A detailed explanation of these factors is given in Chapters 5 and 6.

2.3 $B \to \ell \bar{\nu}_\ell \gamma$: The Structure-Dependent Diagram

Radiative effects in purely leptonic decays should also be investigated. According to the Burdman, Goldman, and Wyler (BGW) model [25], there are two contributions to $B \to \ell \overline{\nu}_\ell \gamma$: the Internal Bremsstrahlung (IB) diagram and the Structure Dependent (SD) diagram. The Feynman diagram for these processes is given in Figure 2.2(b-d). In the IB diagram, a photon is emitted in either the initial or final state. The amplitude for this process is suppressed by both the electromagnetic coupling constant, and the helicity suppression factor.

In the SD diagram, an initial-state photon is produced in the transition of a spin-0 B meson to a spin-1 off-shell vector or axial-vector B meson. Because the heavy intermediate state has spin-1, helicity suppression can be avoided. Hence, the SD process is suppressed only by the electromagnetic coupling.

The decay rate depends on the electromagnetic coupling constant, the mass of the intermediate B meson, and the decay constant of the intermediate B meson. These values are expected to differ for transitions involving vector mesons (B^*s) and axial-vector mesons (B's). In the context of Heavy Quark Symmetry (HQS) [25], the axial vector meson has an orbital angular momentum L=1 and belongs to two separate spin doublets. These states are labelled j=1/2 and j=3/2, the total angular momentum carried by the light degrees of freedom. The mass differences between the excited B meson and the ground-state B meson (Δ^*, Δ_j') are measured directly in the B system [27], and the coupling constants (μ^*, μ_j') are estimated from a combination of charm-system measurements and theory [28]. Therefore, to a first approximation, the only uncertain parameters are the decay constants (f_B^*, f_{B_j}').

HQS cannot relate the decay constants of heavy mesons belonging to different spin doublets [29]; hence, it is useful to define the relative strength of the axial-vector process and vector process as:

$$\gamma_j \equiv \frac{\mu_j' f_{B_j}'}{\mu^* f_B^*} \quad . \tag{2.9}$$

In terms of γ_j, the relative branching fraction of the SD and annihilation diagram is:

$$R_B^\ell = \frac{\mathcal{B}(B \to \ell\bar{\nu}_\ell\gamma)}{\mathcal{B}(B \to \ell\bar{\nu}_\ell)} \tag{2.10}$$

$$= \frac{1}{6\pi}\alpha\mu^{*^2} m_B^2 \left(\frac{m_B}{m_\ell}\right)^2 \int_0^1 dx x^3(1-x) \left\{ \frac{1}{(x+\frac{2\Delta^*}{m_B})^2} + \left(\sum_i \frac{\gamma_i}{x+\frac{2\Delta_j'}{m_B}}\right)^2 \right\}, \tag{2.11}$$

where μ^* is the vector coupling to the photon, Δ^* is the vector B-mass difference, $\Delta_j^{'}$ is the axial-vector B-mass difference, and γ_j is the relative strength of the axial-vector process.

Unfortunately, there are no conclusive experimental indications from other hadronic systems of the relative strength of the axial-vector process, γ_j. We might expect γ_j to be small because, according to non-relativistic models, $f_{B_j}^{'}$ is zero.[2] However, relativistic effects can be important and modify these predictions drastically. If γ_j *is* small, an observation of $B \to \ell\overline{\nu}_\ell\gamma$ would determine f_B^*. Knowledge of f_B^*, together with HQS relation $f_B^* = m_{_B} f_B$ (in units of GeV^2) [30], provides an alternative means to determine f_B.

Due to the absence of helicity suppression, the decay rate for $B \to \ell\overline{\nu}_\ell\gamma$ is expected to be comparable or even larger than $B \to \ell\overline{\nu}_\ell$ decays. This is substantiated by both HQS arguments [31], and Lattice QCD calculations [32]. In addition, to the first order in $(m_\ell/m_B)^2$, the decay rate is independent of the lepton species. Assuming a value for the vector meson decay constant, $f_B^* = 1.0$ GeV^2, the measured value for the B lifetime, $\tau_{\rm B} = 1.6$ ps, and a reasonable estimate of the $b{\to}u$ coupling constant, $V_{ub} = 0.003$ [24], the expected range for the $B \to \ell\overline{\nu}_\ell\gamma$ decay rate is:

$$1.0 \times 10^{-6} \ < \ \mathcal{B}(B \to \ell\nu\gamma) \ < \ 4.0 \times 10^{-6} \ . \tag{2.12}$$

The uncertaintly in this rate is dominated by μ^*, which varies from 1.4 GeV^{-1} to 2.8 GeV^{-1} [33]. The upper limit in Equation 2.12 implies:

$$\mathcal{B}(B \to e\overline{\nu}_e\gamma) \gg \mathcal{B}(B \to e\overline{\nu}_e), \tag{2.13}$$

$$\mathcal{B}(B \to \mu\overline{\nu}_\mu\gamma) \approx 16 \times \mathcal{B}(B \to \mu\overline{\nu}_\mu), \quad \text{and} \tag{2.14}$$

[2] For an orbitally excited state, the wave function of the light quark vanishes at the origin due to the presence of a centrifugal barrier.

$$\mathcal{B}(B \to \tau\overline{\nu}_\tau\gamma) \ll \mathcal{B}(B \to \tau\overline{\nu}_\tau). \tag{2.15}$$

Because the rate for $B \to \tau\overline{\nu}_\tau\gamma$ is a small correction to $B \to \tau\overline{\nu}_\tau$, a decay that is already difficult to detect due to multiple neutrinos in the final state (see Chapter 6), we search for $B \to \ell\overline{\nu}_\ell\gamma$ decays in the channels $B \to e\overline{\nu}_e\gamma$ and $B \to \mu\overline{\nu}_\mu\gamma$. A complete description of these analyses is given in Chapter 7.

Chapter 3

The Experiment Apparatus: CESR and CLEO

The data used in this thesis were obtained using the Cornell Electron Storage Ring (CESR), and the CLEO II detector. This chapter describes the production of B mesons using the CESR facility, and the detection of B-meson decays using the CLEO II detector.

3.1 CESR

CESR is a high energy electron-positron collider located approximately 50 feet beneath the campus of Cornell University in Ithaca, New York. The entire facility is approximately 1/2 mile in circumference, and consists of three main parts: (1) the linear accelerator, (2) the inner synchrotron ring, and (3) the outer storage ring (see Figure 3.1).

3.1.1 Beam Production

The acceleration and production of electrons and positrons begins in the linear accelerator, or *linac*. Electrons are produced by a hot-cathode electron gun near the beginning of the linac, and accelerated by a continuous line of small radio frequency (RF) cavities to approximately 150 MeV. In a separate procedure, positrons are produced by directing the electron beam into a thin tungsten target located half way down the linac. Through the process of bremsstrahlung (or radiation loss) and pair production, a shower of low energy electrons and positrons are produced. The positrons are then focused, and accelerated down the remainder of the linac.

Both the electrons and positrons are injected into the inner synchrotron ring.[1] The synchrotron accelerates the electrons and positrons in circular orbits to approximately 5 GeV using an additional set of RF cavities. At an energy of 5 GeV, electrons and positrons travel at 99.9999995% the speed of light.

A periodic arrangement of dipole and quadrupole magnets in the synchrotron is used to keep the particles in stable orbits and confine them into several ribbon-shaped bunches. Each bunch contains approximately 2×10^{11} particles in a volume with dimensions: width = 0.6 mm, height = 0.011 mm, and length = 17 mm [34]. The electron and positron bunches rotate in opposite directions. After the particles have been sufficiently accelerated, they are transferred to the outer storage ring.

The outer storage ring functions in the same way as the synchrotron, except that the RF cavities are used to restore energy lost due to synchrotron radiation.[2] Under typical running conditions, the electrons and positrons are grouped into 7 bunches each. The bunches orbit at 390 kHz and have an energy spread of approximately 0.06%. As the

---

[1] In practice, the positrons are injected first, and the electrons second.

[2] Energy loss due to synchrotron radiation (approximately 0.5 MeV per orbit) appears in the form of very intense and well-focussed x-rays. A parasitic facility called CHESS (Cornell High Enrgy Synchrotron Source) allows chemists, biologists, and other scientists to exploit this phenomenon [35].

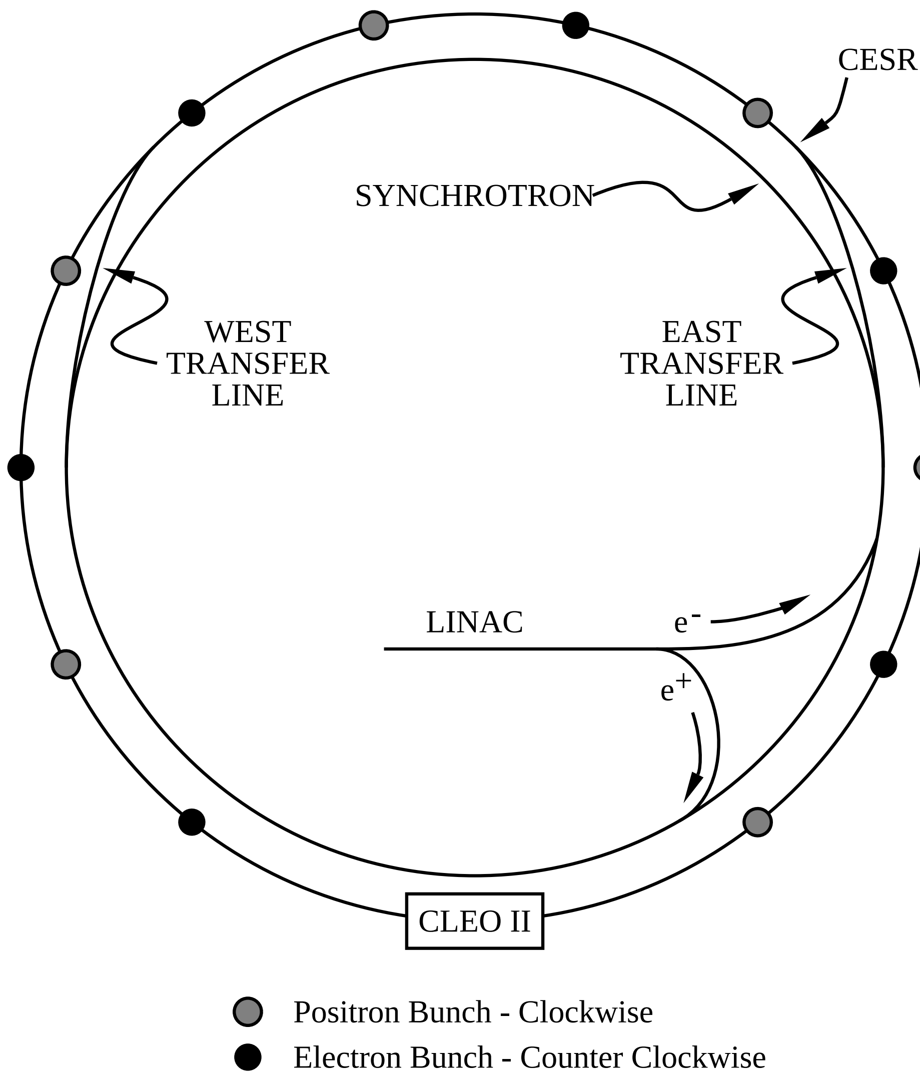

Figure 3.1: A schematic diagram of the main components of the CESR facility as viewed from above.

bunches orbit the ring, they are forced into oscillations about the center of the beam pipe. In this configuration, the bunches interact at only one point located at the center of the CLEO II detector. This point is called the interaction region.

3.1.2 Luminosity Measurement

The rate of collisions between bunches in the interaction region is given by:

$$\mathcal{L} = nf\frac{N(e^+)N(e^-)}{A(e^+e^-)}, \tag{3.1}$$

where $N \approx 10^{11}$ is the number of particles in a bunch, $A(e^+e^-) \approx 5 \times 10^{-4}$ cm^2 is the effective area of the beams, and $f \approx 400$ kHz is the orbital frequency. The number of bunches n was 7 for most of the data. Typical peak luminosity at CESR during this period of operation was $\mathcal{L} = (1-3) \times 10^{32}$ cm^{-2}s^{-1}. The cross section for a given scattering process is then given by:

$$\sigma \equiv \frac{\mathrm{N}}{\int \mathcal{L}dt}, \tag{3.2}$$

where the numerator, N, is the total number of scattering events, and the denominator is the total integrated luminosity.

3.1.3 Υ(4S)-Resonance Production

When an electron-positron collision occurs, the electron and positron may simply scatter off one another, or annihilate into a virtual photon which may materialize as a particle-antiparticle pair. The result of each collision is called an *event*. The first-order decay diagram for the annihilation process is shown in Figure 3.2. If the total electron-positron collision energy is equal to the mass of a meson (carrying the same quantum numbers as the photon), the cross section for this process is enhanced. An enhancement in the cross section is called a *resonance*.

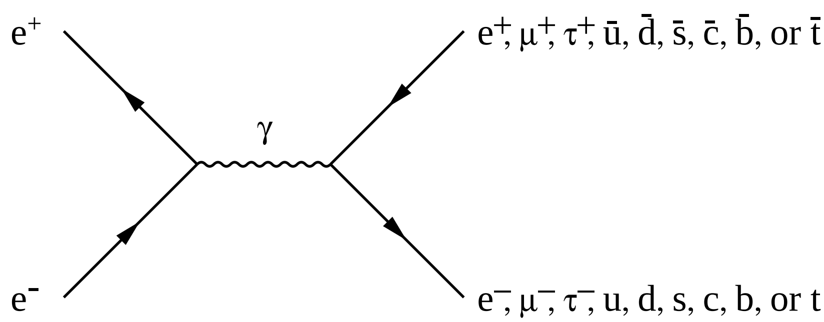

Figure 3.2: e^+e^- annihilation, and all possible final state particles.

Four such resonances are observed in the hadronic cross section near 10 GeV (see Figure 3.3).[3] These resonances are labelled Υ(1S), Υ(2S), Υ(3S), and Υ(4S), and correspond to the ground state and excited states of a $b\bar{b}$ system, respectively [36]. The natural width of the first three resonances ($\approx$ 40 KeV) is dominated by the beam-energy resolution ($\approx$ 6 MeV). In contrast, the natural width of the fourth resonance (14 MeV) is comparable to the beam-energy width. The relative narrowness of the first three resonances and the fourth resonance is ascribed to the so-called Zweig (or OZI) rule where decays of $b\bar{b}$ mesons are suppressed by unconnected lines in the quark flow diagram [37].

As can be seen from Figure 3.3, the four resonances sit on top of a nearly flat background. This background can be divided into three main parts: (1) $q\bar{q}$ pairs, where $q = d, u, s,$ or$c$, (2) $\mu^+\mu^-$, $\tau^+\tau^-$, plus higher order QED processes, and (3) two-photon collisions. Two-photon collisions occur when the electron and positron each radiate a virtual photon; the photons may then interact, producing a large amount of hadronic

[3]The event selection criteria used to select hadronic events are given in Section 5.2.3.

energy [38]. The total hadronic background is referred to as the "continuum".

The data used in this thesis were collected at the $\Upsilon(4S)$ resonance at the center of mass energy $\sqrt{s} = 10.58$ GeV. This data sample is referred to as the "on-resonance sample". Unlike the lower energy upsilon resonances, b quarks at the $\Upsilon(4S)$ are only loosely bound and may move away from each other; as they separate, the strong force between the quark results in the creation of a light quark-antiquark pair ($u\bar{u}$ or $d\bar{d}$). The quarks group together to form a pseudoscalar B meson and anti-B-meson (see Figure 3.4). Each B meson has a mass 5.28 GeV and is produced nearly at rest ($\beta = 0.06$). The $\Upsilon(4S)$ is believed to decay only to $B\overline{B}$, making it possible to obtain a very well-understood sample of B mesons.

Data are also collected below the $\Upsilon(4S)$ resonance at $\sqrt{s} = 10.52$ GeV. This sample contains only continuum processes (see Figure 3.2). Since this sample cannot contain B decays, it is used to estimate the continuum contribution to the $\Upsilon(4S)$ resonance. The on- and off-resonance samples are described in more detail in Section 5.2.2.

3.1.4 Beam Decay

As electrons and positrons interact and produce interesting physics, the beams themselves begin to die out. Particles may, for example, collide with residual gas, an effect significantly reduced by maintaining a high vacuum (10^{-8} torr) in the storage ring [40]. Particles may also drift out of orbit and collide with the beam-pipe walls, or become lost in a collisions at the interaction region. Such effects limit the storage time of the beams to approximately two hours. The beams are rejuvenated approximately once per hour.

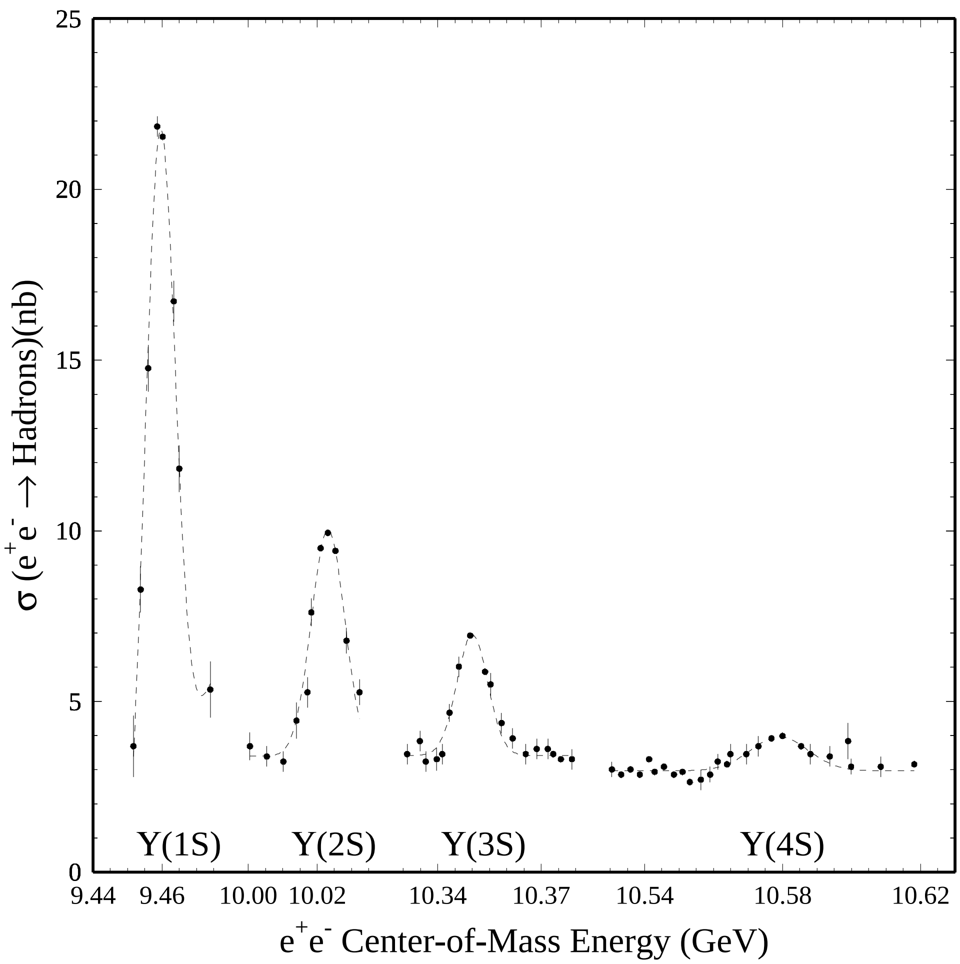

Figure 3.3: The hadronic cross section of e^+e^- annihilations in the Υ energy region.

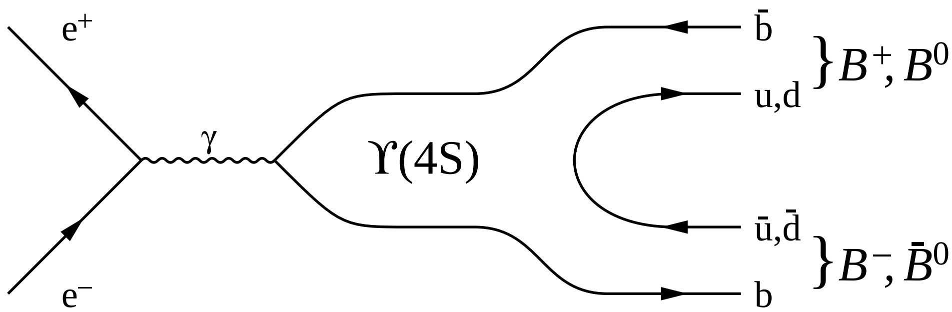

Figure 3.4: Production of B mesons in e^+e^- collisions.

3.2 The CLEO II Detector

The CLEO II detector is positioned at the interaction region of CESR. The purpose of CLEO II is to simulataneously measure the trajectory, momentum, energy, and identity of each particle in an event. To detect particles that emerge in any direction, the interaction point is surrounded by detector components. Consequently, CLEO II is a very large apparatus, occupying a space six meters long, eight meters wide and nine meter high, and weighing 1.5 million kilograms [41].

3.2.1 B-Decay Measurements

Once a $B\overline{B}$ pair is produced by CESR, each B decays via the weak interaction (within a few pico seconds), producing a spherical spray of charge and neutral particles throughout the CLEO II detector. Among the particles that are detectable are: $e^{\pm}$, $\mu^{\pm}$, $\pi^{\pm}$, $K^{\pm}$, p and $\bar{p}$, and the neutral particle γ. Other particles that decay too quickly to be *directly* observed, but that can be inferred from their decay products, include the charmed mesons ($D^{\pm}$, D^0, $\bar{D}^0$, $D_s^{\pm}$), the $\tau^{\pm}$ lepton, and many other mesons and baryons ($\Lambda_c^{\pm}$, J/ψ, π^0, K_s^0, $\Lambda^{\pm}$, ϕ, ρ, etc.). For example, the decay $\pi^0 \to \gamma\gamma$ is recognized by comparing the invariant mass of a detected pair of photons with the known π^0 mass. Other particles are either too difficult (n and K_L^0) or impossible (ν_e, ν_μ, ν_τ) to detect with CLEO II.

Ideally, enough measurements can be performed to either partially or fully reconstruct a B meson. The first evidence for the existence of the B meson came from the partial reconstruction of "semileptonic" decays. These decays occur when a B decays into a muon or an electron, together with a neutrino and one or more hadrons. Since the leptons are produced singly and not in oppositely charged pairs, backgrounds from QED processes can be ruled out. Moreover, the observed lepton momenta were consistent with coming from a heavy B meson, and not from a lighter charged or strange meson. Similar measurements have since been performed for many common ($B \to D^*\pi$, $B \to J/\psi K$, etc.) and rare ($B \to K^-\pi^+$, $B \to \pi^+\pi^-$, $B \to K^*\gamma$, etc.) B-decay processes. The current CLEO II dataset includes a large sample of both partially and fully reconstructed B mesons [42].

3.2.2 Detector Overview

The CLEO II detector is described in cartesian and cylindrical coordinates. The z axis extends in the beam direction, the y axis in the up direction, and x axis in the inward-radial direction. The x-y or r-ϕ plane is perpendicular to the beam line.

At the core of the CLEO detector (see Figure 3.5 and Figure 3.6) is a superconducting solonoid magnet, approximately 1.5 meters in radius and 3.5 meters long. Inside the magnet is a cylindrical drift chamber which detects tracks of charged particles emerging from the interaction region. As many as 67 separate measurements are made to determine the complete trajectory of each charged track. The curvature of each track within a nearly uniform 1.5 Tesla magnet field is used to determine the track momentum. These chambers also provide measurement of the energy loss over the length of each track. Measurements of energy loss provide the velocity of a track, and may be combined with the track momentum to determine the mass or identity of each track.

Just beyond the tracking chambers is a system of plastic scintillation, or time-of-flight (TOF), counters. As particles cross the TOF counters they produce flashes of light. The light is collected and detected by photo-multiplier tubes and used to determine the arrival time of each track. This information can be combined with known beam crossing time to determine the velocity of each particle. As mentioned before, velocity information is used for particle identification.

Charged and neutral particles passing through the TOF counters enter the CsI crystal calorimenter. Here, photons and electrons deposit all their energy in the form of electromagnetic showers. Other particles such as muons and hadrons often deposit very little energy and pass into the muon iron. The energy of each electromagnetic shower is determined from the light collected by the crystals. For photons, the size and location of the shower translates directly into the energy and direction information (provided that the photon originates from the interaction point). For charged particles, the size of shower can be combined with the momentum of the corresponding track to identify electrons.

Outside the coil of the solonoid magnet is a thick set of iron muon chambers. Most hadrons are filtered away when they interact via the strong interaction with the iron. To a good approximation, the only particles that reach the muon counters, and create hits in the muon chambers, are muons.

Below, each CLEO II detector component is described in detail, beginning from the central region of the detector and moving outward. A more complete description of the CLEO II detector can be found in Reference [43].

3.2.3 The Beam Pipe

The interface between the CESR vacuum and CLEO II is a beryllium pipe. The pipe is 500 μm thick, 33 cm long, and 7 cm in diameter. The inner face of the pipe has a 20-μm

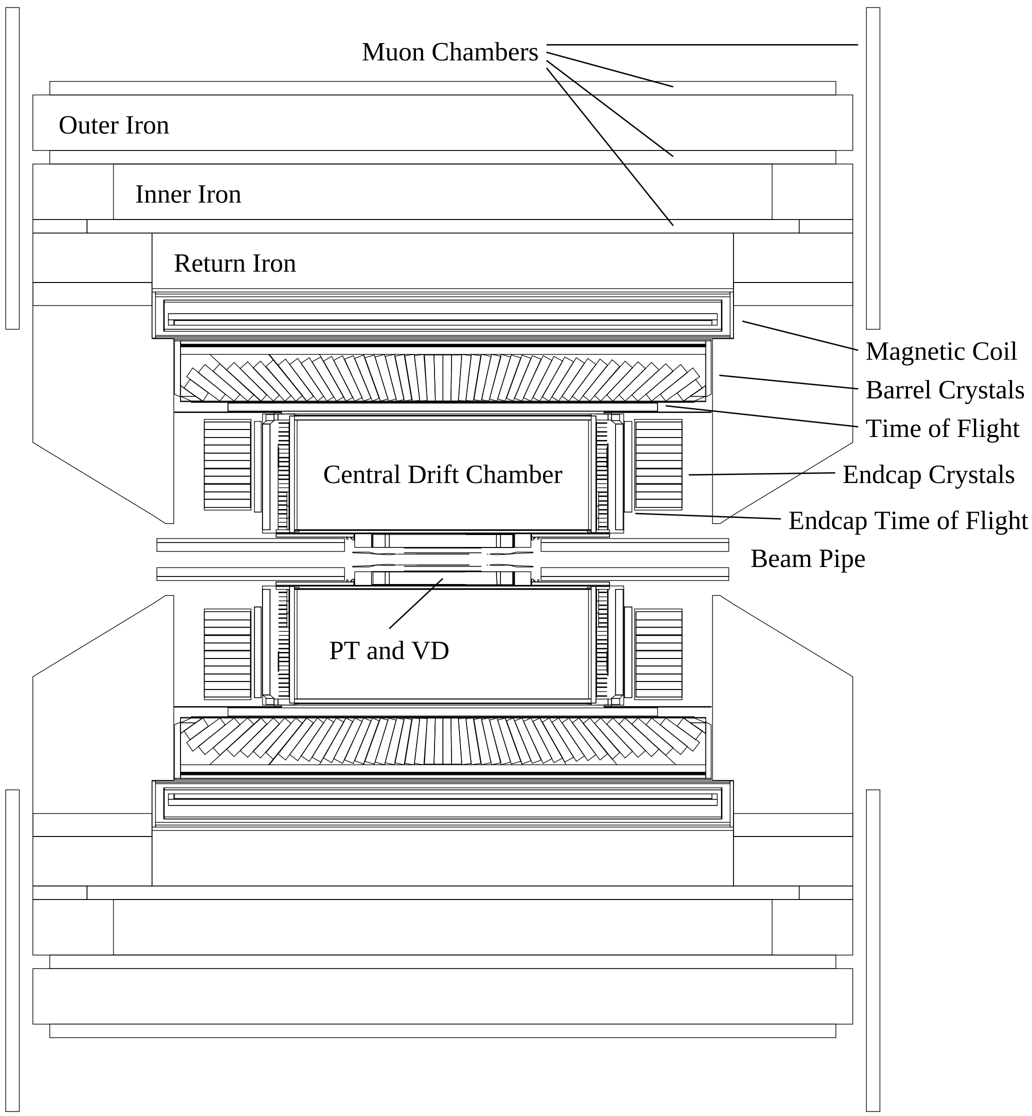

Figure 3.5: A side view of the CLEO II detector. The central detector consists of three concentric drift chambers: the precision tracker (PT), the vertex detector (VD), and the central drift chamber. The "Return Iron" of the muon system serves as most of the return yoke of the magnet.

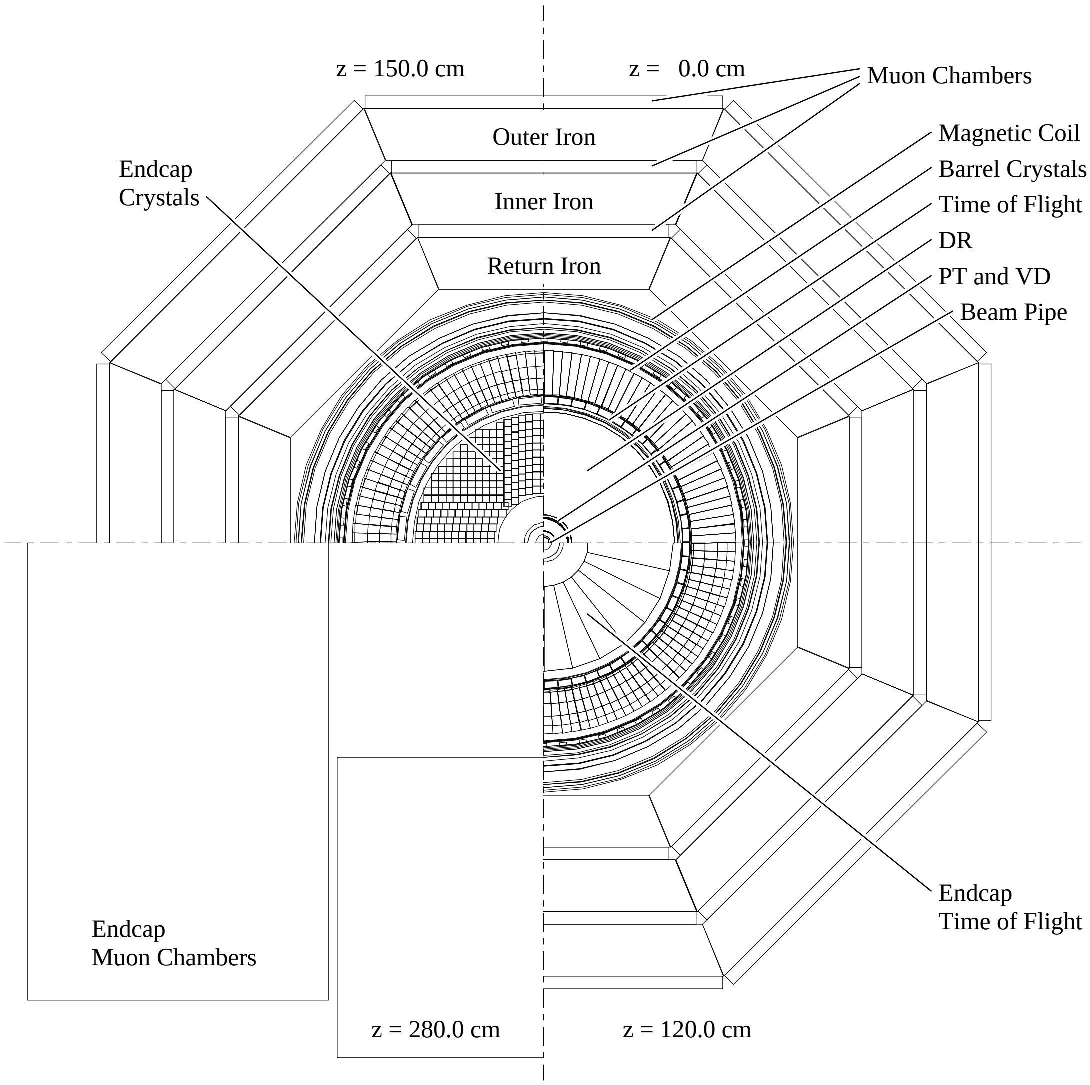

Figure 3.6: An end view of the CLEO II detector.

layer of silver and a 1-μm layer of nickel. These layers prevent synchrotron radiation from entering CLEO II. The pipe covers a solid angle of 99% of 4π, constitutes 0.44% of a radiation length to normally-incident particles.[4] Particles emerging in the direction of the beam line, typically strike either the support structure of the tracking chambers or the magnets within CESR.

3.2.4 The Central Detector

The central detector consists of three concentric drift chambers: the precision tracker (PT), the vertex detector (VD), and the central drift chamber (DR). Each tracking chamber contains a different array of anode wires that run parallel to the beam pipe. The anode wires are surrounded by cathodes which are used to shape the electric fields (the location and type of cathode used varies from chamber to chamber). The cathodes define a "drift cell" at each anode. As charged particles spiral outward under the influence of the magnetic field, they interact with a gas in each chamber. These interactions produce ion pairs (positive ions and electrons). While the electrons drift toward the nearest high voltage anode wire, the positive ions drift more slowly away from the wire. The paths of the electrons are influenced by the detailed features of the magnetic and electric fields around the wire. Contours of equal drift time are called "isochrones", and may be different from cell to cell. As the electrons near to the anode wire they accelerate dramatically and produce additional ions. This process results in a chain reaction, or cascade, which produces an electronic signal at the anode. The rising edge of this signal can be used to determine the drift time of the electron. The electron drift time, together with a knowledge of the isochrones, can be used to determine the distance of closest approach of the charged particle to the anode. A series of such measurements can be used to determine the trajectory of the particle.

[4] One radiation length is the thickness of a material necessary to reduce the average energy of a beam of electrons (excluding electrons produced in showers) by a factor $1/e = 1/2.718$ through bremsstrahlung [44].

Drift chambers may also be used for particle identification. This can be accomplished by operating the drift chamber in proportional mode. In this mode, the magnitude of the electronic pulse is proportional to the total number of primary electron-ion pairs which is related to the ionization loss of the charged particle.

The Precision Tracking Layer (PT)

The precision tracking layer (PT) is the innermost detector component of CLEO II (see Figure 3.7). The objective of the PT is to measure the central vertex of each charged track as precisely as possible. The PT uses a six-layer straw tube drift chamber. The tubes are mounted around the beam pipe in a hexagonal packing arrangement. Each tube is 50 cm long, 2.5-3.5 mm in diameter (depending on the distance from the interaction region), and is composed of a piece of aluminized mylar. While each tube serves as a cathode, a wire drawn down the center of each tube serves as an anode. The gas uses in the PT depends on the dataset. The first half of the dataset uses a 50:50 mixture of argon and ethane (at atmospheric pressure), and second half of the dataset used Dimethyl Ether (DME). The active region of the PT covers a radial distance of 4.5-7.5 cm. The entire structure is covered by an additional layer of mylar and is held together by a layer of epoxy.

The r-ϕ resolution of the wires is $\approx$100 μm (argon-ethane) or $\approx$60 μm (DME), when averaged over the entire tracking volume (the PT cannot make measurements in the z direction). The efficiency for detecting a track at an anode wire is 85% (argon-ethane) when averaged over an entire cell. The PT presents a total of 0.28% radiation lengths to normally-incident particles.

The Vertex Detector (VD)

The vertex detector (VD) extends from 8.0 to 16.6 cm in the radial direction, and from -35.0 to 35.0 cm in the z direction. The VD contains 10 layers of very closely spaced anode wires, 5 layers of 64 wires and 5 layers of 96 wires. The cathodes are provided

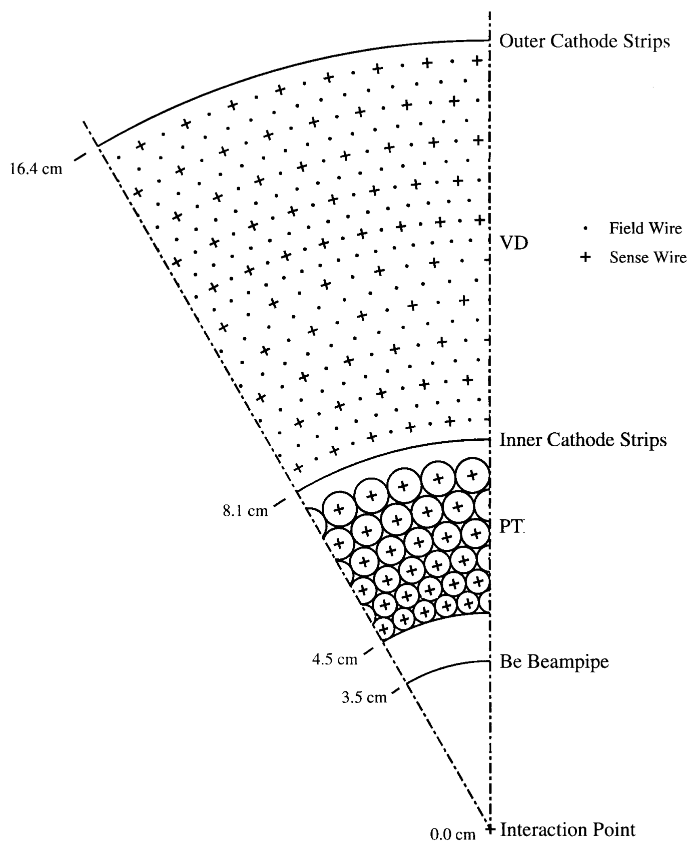

Figure 3.7: An end view of the inner tracking chambers showing the pattern of wires and their radii.

by a series of field-shaping wires arranged hexagonally about each anode, or sense wire. This hexagonal structure provides nearly circular isochrones which simplify tracking measurements. The anode wires are made from a high resistance nickel-chromium wire. This allows the measurement of charge ratio (charge division) at the two ends of the wire, which can be used to determine the z position of the track. Charge division techniques were used for approximately 90% of the data used in this thesis. As for the PT, the VD uses a 50:50 argon and ethane gas mixture, but at higher pressure (20 psi) to reduce the effect of diffusion on the spatial resolution [45].

The performance of the VD is further enhanced by a set of cathode strips on the inner and outer walls of the VD. The cathode strips are made of carbon filament tubes lined with aluminum-coated mylar. The mylar is 75 μm thick, and the aluminum coat is 8 μm thick. Each tube serves as a cathode. The cathodes are segmented into 8 strips in the ϕ-direction and 64(96) strips in z direction along the inner(outer) walls. When a charged particle interacts with the gas near the inner or outer walls, positive ions induce an image charge on the cathodes. This provides additional information for ϕ and z-position measurements.

The VD has an average r-ϕ resolution of 150 μm. The z resolution is $\approx$ 1.2 cm using charge division, and 750 μm using the cathode strips. The efficiency for registering a hit in a cathode strip is about 83(78)% for the inner(outer) layer.

The Central Drift Chamber (DR)

The central drift chamber (DR) provides the most tracking information of the tracking chambers. The DR extends from 17.8 to 94.7 cm in the radial direction, and from -94.5 to 94.5 cm in the z direction. The DR contains 12,240 sense wires and 36,240 field wires, which are arranged into square drift cells. Two large 1.25 inch thick aluminum plates support the wires at each end. As in the VD, the inner and outer walls of the DR are lined with cathode strips. The outer shell of the DR is made from a plastic honeycomb sandwiched between 1/32-inch thick layers of aluminum, which provides support for the end plates. The inner shell is lined with a thin layer of graphite epoxy to prevent gas leakage.

As shown in Figure 3.8, there are 51 concentric layers of sense wires. The number of sense wires per layer increases from 96 in the inner layer to 384 in the outer layer, providing a constant cell size (15 mm by 15 mm) throughout the drift chamber. Each square cell consists of a gold-plated 20 μm tungsten sense wire, and 8 surrounding field wires [46]. The field wires are made of aluminum in the first forty layers, to reduce multiple scattering, and copper-beryllium in the remaining layers. The small size of the anode wires is chosen to increase the gas amplification factor (if the wire is too *small*, frequent wire breakage occurs). The sense wires are used to measure both the drift time and ionization energy loss of each passing particle.

Every fourth layer contains stereo wires. Stereo wires are tipped with respect to the z-axis to provide z-position information. The angle the stereo wires make with the z-axis ranges from 3.8° to 6.9°. The sense and field wires between each stereo layer form an “axial layer”. Wires within an axial layer line up radially, and wires in adjacent axial layers are staggered by a half-cell in the azimuth. Staggering each sucessive axial layer helps resolve ambiguities associated with the relative position of the track and anode wire in the preceding axial layer.

Both the inner and outer cathodes are made of aluminum-coated mylar sheets. The inner cathode is segmented into 96 sections in the z direction, and 16 sections in the ϕ direction. The outer cathode is segmented into 192 sections in the z direction, and 8 sections in the ϕ direction.

The DR has an average r-ϕ resolution of 150 μm. The z resolution in each stereo layer varies from 3-6 mm (assuming at least 3 of the 12 possible stereo layers is hit). The z resolution provided by the inner cathode strips is 1 mm, with a solid angle coverage of 92% of 4π. The z resolution provided by the outer cathode strips is 600 μm, with a solid angle coverage of 71% of 4π.

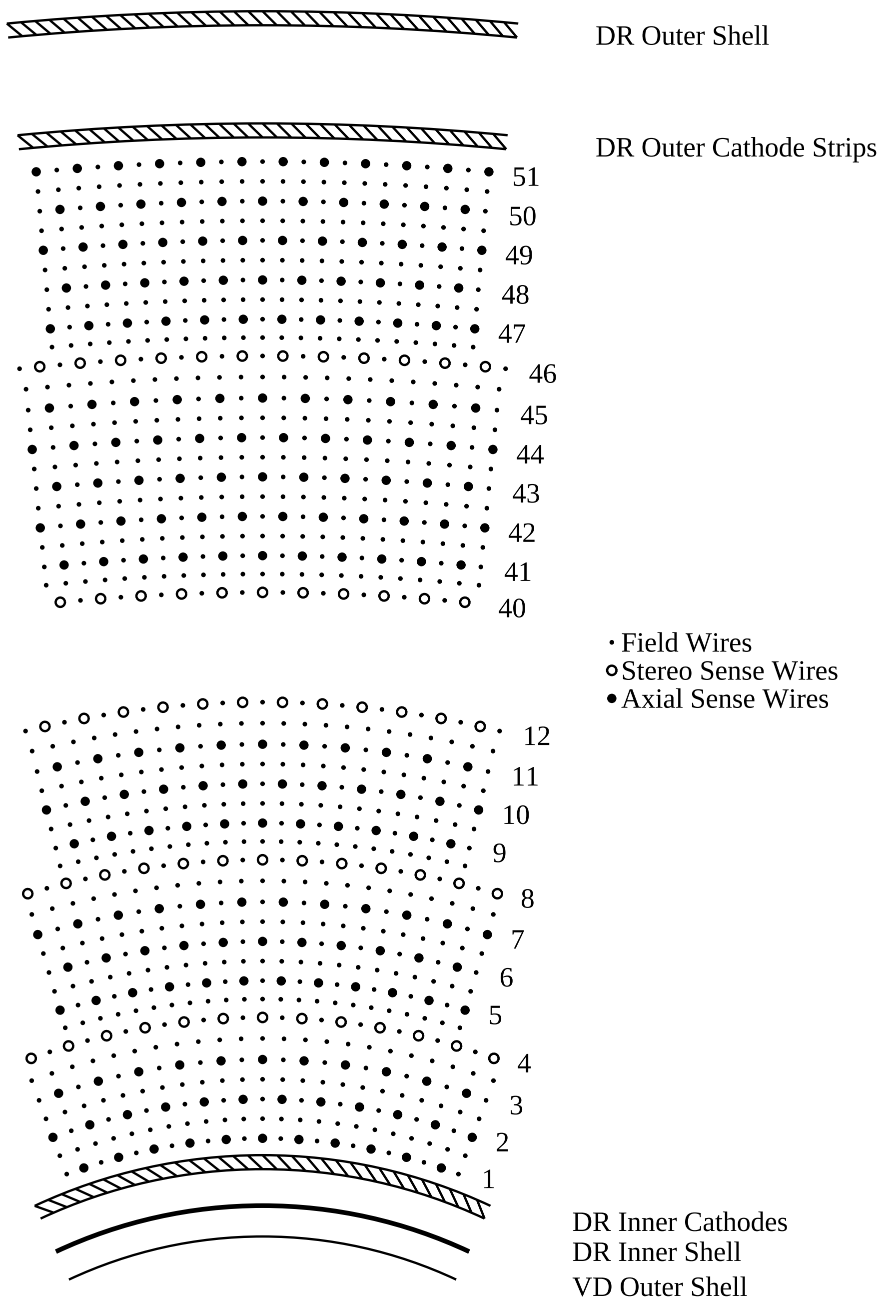

Figure 3.8: The wire positions and structure of the central drift chamber.

3.2.5 The Time-of-Flight Detector (TOF)

Just beyond the tracking chambers is a system of plastic scintillation, or time-of-flight (TOF), counters. Each plastic counter is doped with organic molecules. Particles that enter the counters excite organic molecules in the plastic. As the molecules return to ground state, they release ultraviolet light. This process is called *scintillation*. The ultraviolet light is then converted to blue light by embedded dye molecules. The resulting light reflects internally down the length of the scintillator into a plastic light pipe leading to a photomultiplier tube. Information collected with the phototubes are used to determine the arrival time of each particle.

The TOF system has two primary functions. First, the TOF system is used for particle identification. As described in the detector overview, the arrival time of each track can be combined with the measured track momentum to determine the mass, or identity, of the particle. Second, the TOF system is used by the CLEO II trigger system (see Section 3.2.9). The fast response time of the TOF system is used to recognize the occurence of an interesting events at each bunch crossing.

The TOF system is composed of two parts: the barrel and the endcap. The barrel TOF system contains 64 strips of 5-cm thick Bicron BC-408 scintillator. Mounted to the end of each scintillator is an ultraviolet-transparent light guide made of lucite and an Amperex XP2020 photomultiplier tube. The phototubes operate in a low-field environment beyond the return flux of the magnet.

The endcap TOF system contains 28 counters. The endcap counters are made from 5-cm thick trapezoidal-shaped scintillators. The counters are 58-cm long and are read out at the narrow end. Design difficulties in the endcap light guides made it necessary to position the phototubes inside the magnetic field. Hamamatsu R2580 phototubes are used which are insensitive to axial magnetic fields, though their gain is much lower.

The time resolution of the barrel TOF system is approximately 160 picoseconds per

Table 3.1: The cumulative material in the inner portions of the CLEO II detector at $\theta = 90°$ measured in radiation lengths.

Region	Cumulative Material (in radiation lengths)
Layer 1 of the PT	0.46%
Layer 1 of the VD	1.38%
Layer 1 of the DR	2.5%
Outside the DR outer shell	6.0%
Outside the TF	16.5%
The front of the CC	18%

tube, average over all particle types. The time resolution of the endcap TOF is approximately 200 picoseconds for Bhabha electrons.[5] The combined solid angle coverage of the barrel and endcap TOF counter is 97% of 4π.

3.2.6 The Electromagnetic Calorimeter (CC)

The CLEO II electromagnetic crystal calorimeter (CC) is system of 7800 thallium-doped cesium iodide crystal blocks located outside the TOF counters. Like the TOF system, the CC has both barrel and endcap detectors. The amount of material each particle must traverse before reaching the CC is given in Table 3.1. Charged particles and photons that enter the CC deposit energy into the crystals. The release of energy across many crystals is called a shower. The calorimeter is built of a high-Z material to contain showers with a small volume. The shower light is collected by photodiodes at the back of the crystals and used to determine the energy and location of each shower.

High energy electrons interact with the calorimeter in a very dramatic way. As they pass into the CC, they immediately scatter against heavy nuclei in the crystals and release energy in the form of radiation, a process known as *bremsstrahlung* (or radiation

[5] For comparison, light travels 6 cm in 200 picoseconds.

loss). The photons emitted in bremmstrahlung may then interact with additional nuclei and produce electron-positron pairs. These pairs may also bremsstrahlung. The ensuing chain reaction, or cascade, continues until the average electron energy is so small that other processes such as ionization loss begin to dominate. In the end, almost all the incident electron energy is deposited in the calorimeter.[6] The result is the production of an electromagnetic shower in the calorimeter. Likewise, high energy photons also deposit their incident energy as electromagnetic showers in the CC. In this case, the cascade is initiated by pair production.

Other particles, such as muons and pions, rarely produce cascade showers, since the cross section for bremmstrahlung is suppressed for heavy particles. Typically, muons and hadrons lose energy through ionization, a process dependent only on the particle velocity. Occasionally, charged and neutral hadrons interact by the strong force with the crystal nuclei and produce larger, more diffuse showers. The use of CC to detect and measure hadrons is discussed in Sections 4.3 and 4.4.4.

The barrel calorimeter contains 6144 crystal blocks, each approximately 30 cm long and 25 cm^2 in cross section, which are arranged in a center-pointing geometry.[7] The crystals are divided into 128 sections in the ϕ-direction, and 48 crystals in the z direction. Likewise, the endcap contains 828 rectangular crystals stacked in a large ring. All crystals are held firmly in place by an aluminum "egg-crate".

Each crystal presents 16 radiation lengths to electrons and photons, preventing shower leakage out the back of the crystals. The crystals are wrapped in 0.12 mm thick white teflon for large reflectivity and wrapped in 0.01 mm thick aluminized mylar to create a light seal between adjacent crystals. Four Hamamatsu S1723-06 photodiodes are mounted on 6-mm thick UVT lucite wafers at the back of each crystal. Each crystal

[6] This fact is exploited to identify electrons (see Section 4.4.3).

[7] Actually, the crystals in the barrel CC are only *approximately* center-pointing to prevent photons from slipping through cracks between the crystals.

Table 3.2: The energy resolution of the CsI calorimeter in response to 5 GeV/c Bhabha electrons, and the angular limits of different regions of the calorimeter (1996). The effect of radiation in the sample events is not subtracted.

Region	Angular Region	Solid Angle (% of 4π)	Resolution (%)†
Good Barrel (GB)	$45°$ - $135°$	70.7	1.3
Bad Barrel (BB)	$37°$ - $45°$	9.2	2.7
Overlap (OB)	$30°$ - $37°$	6.7	7.6
Good Endcap (GE)	$25°$ - $30°$	4.0	3.2
Bad Endcap (BE)	$18°$ - $25°$	4.5	5.3

† The energy resolution is defined by σ_E/E, where σ_E = FWHM/2.35 [68].

can function properly with only one diode. Given the diode failure rate of 40 per year, it will take approximately 75 years before one crystal loses all four diodes.

The energy resolution of the calorimeter is strongly dependent on the detector region (see Table 3.2). The energy resolution of the "bad barrel" region is impaired by the DR endplate (3-cm thick aluminum), voltage cables, pre-amps, and a copper cooling plate (3-mm copper). The energy resolution of the "overlap" region (i.e. the region where the barrel and endcap crystals overlap) is degraded by the endcap support structure, and a smaller crystal radiation length. The endcap resolution is degraded by the drift chamber endplate and electronics, and by shower leakage out the edges of the bottom crystals. Criteria for reading out CC electronics and combining crystal hits into showers are described in Sections 3.2.9 and 4.3.1.

3.2.7 The Superconducting Magnet

The tracking chambers, TOF system, and CC are surrounded by a superconducting coil which provides a uniform 1.5 Tesla magnetic field in the z direction. The Lorentz force produced by the magnetic field bends each charged particle into a curved path, or helix. The radius of the helix is used to determine the momentum of the charged track (see Section 4.2).

The coil consists of two layers, each with 650 turns of cable. The cable is made of a high purity aluminum stabilizer, which contains a niobium-titantium-copper wire. The inner diameter and length of the coil is 2.9 m and 3.5 m, respectively. The magnetic flux return is facilitated by a 800,000-kg steel yoke that is also used by the muon identification system. The magnet is cooled with liquid-helium stored in a reservoir above the detector.

The uniformity of the magnetic field is measured using a Hall probe, and is shown in Figure 3.9. Variations in the field strength are monitored continuously by an an NMR probe and are stable to 1 Gauss.

3.2.8 The Muon Identification System (MU)

The outermost detector component of CLEO II is the muon identification system (MU). The MU system also consists of a barrel and endcap detector. The barrel detector is divided into 8 octants, each containing three thin "superlayers" of proportional counters interleaved with 30 cm thick iron slabs. The endcap calorimeter contains one thin superlayer. Muons can penetrate much deeper into the iron than other particles since they are both heavy and immune to strong interactions. For this reason, the MU system is often called a "muon filter".

A superlayer consists of *three* layers of plastic proportional counters, operating at 2,500 V, within a 50:50 argon-ethane mixture (see Figure 3.10). The redundancy of layers insures the MU system against malfunctions. Each counter is about 5 m long, and 8.3 cm wide, and is divided into eight 0.9 cm by 0.9 cm rectangular drift cells. The sides of each cell are coated with graphite and serve as a cathode; a silver-plated Cu-Be wire strung down the center of each cell serves as an anode. The eight anodes are connected together, each separated by a 100-Ω resistor, giving a spatial resolution of 2.4 cm. This resolution is better than the spatial uncertainty for multiple scattering for high-momentum muons, the particles of interest in our experiment. Wires belonging to

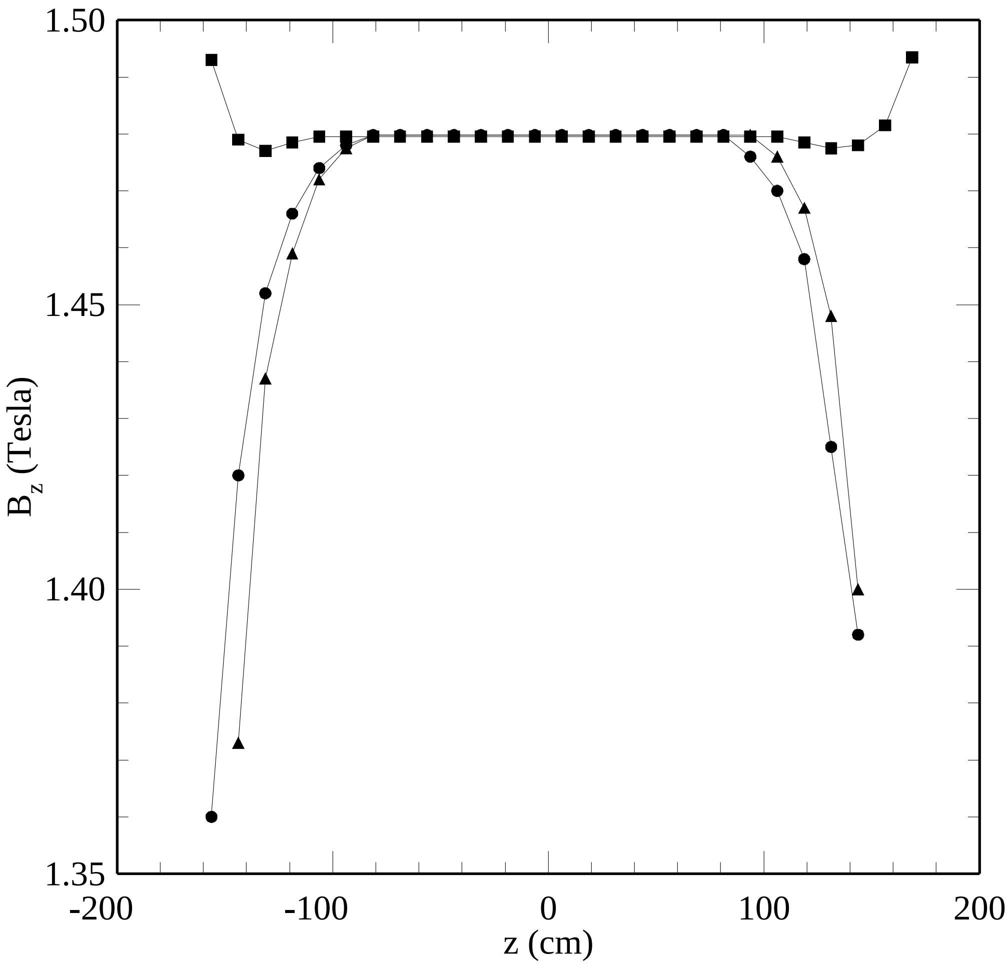

Figure 3.9: A plot showing the z component of the CLEO II magnetic field as a function of z position at 3 different radii. The triangles, circles, and squares show the field at radii of 0.6 cm, 19.4 cm, and 69.4 cm, respectively.

Table 3.3: The solid angle coverage of the various barrel muon counters and their efficiency for detecting 5 GeV/c muons.

Muon Layer	Solid Angle (%)	Efficiency (%)
Return	$0.85 \times 4\pi$	0.99 ± 0.01
Inner	$0.82 \times 4\pi$	0.98 ± 0.01
Outer	$0.79 \times 4\pi$	0.90 ± 0.02

counters in different layers are staggered to reduce geometrical tracking inefficiencies. Copper cathode strips outside the cell run perpendicular to the wires and provide a z-position resolution of 5.3 cm.

The solid angle coverage and hit efficiency for 5 GeV barrel muons is given in Table 3.3. The solid angle coverage is limited by the protruding light guides of the TOF system. Barrel muons must have at least 0.8 GeV/c to reach the first superlayer.

3.2.9 The Trigger System

The CLEO II trigger system uses the fastest components of the CLEO II detector to determine if a given event is worth keeping. Since the CESR bunch-crossing frequency is approximately 2.8 MHz, and the actual rate of interesting collisions is about 10 Hz, the trigger system lifts an enormous burden off of the CLEO II data aquisition system. Even with this system, approximately 2 gigabytes of data are written to tape per day.

The trigger system contains three triggers: L0, L1, and L2. Each trigger contains separate *trigger lines* that correspond to different combinations of detector data used for event-selection. A trigger line “fires” when the input indicates the occurence of an interesting event. When this occurs, additional data are prepared for analysis by the next trigger. Each trigger corresponds to a successively tighter set of event-selection criteria. The main requirements to pass *all three triggers* is that energy is deposited in the TOF system and CC, and more than one track is found in the DR.

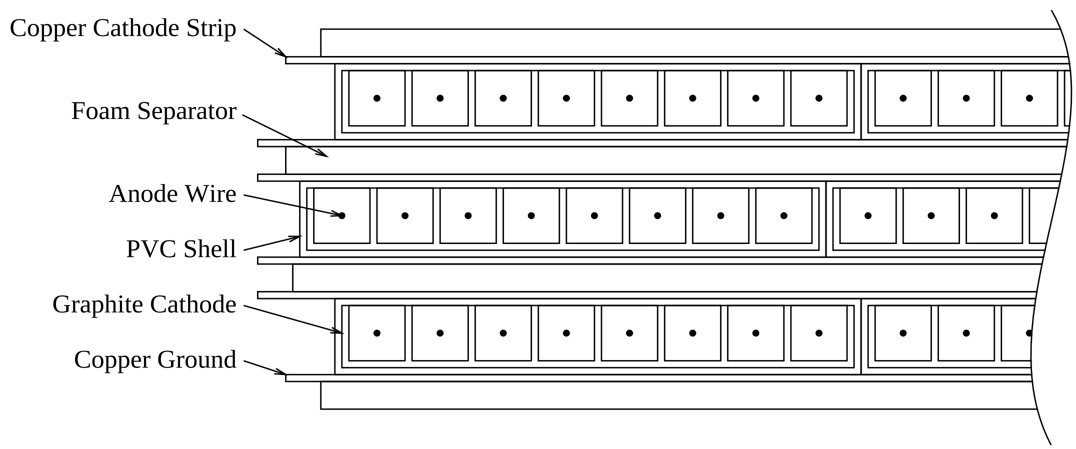

Figure 3.10: Cross section of a muon super layer. (Courtesy of Jeff Nelson of the CLEO Collaboration.)

The L0 trigger uses information from the TOF system, the VD and the CC. When the L0 trigger fires, sample-and-hold circuits are used to "freeze" the data until the event either fails the L1 or L2 requirements, or the system has been read out. Since the L0 trigger must make a decision each time the bunches cross, this trigger must use only the fastest parts of the detector. The TOF is the fastest of these devices. The signals from the TOF phototubes register in only 55 ns. The L0 trigger rate is approximately 10 kHz.

The L1 trigger uses information from the TOF system, VD, CC, and DR. Preparing data for L1 takes approximately 1.5 μs. This introduces a dead time of 2% (which must be used to correct the estimated integrated luminosity). If the L1 trigger fires, additional data are prepared for the L2 trigger; if not, the detector is reset for the L0 trigger. The L1 trigger rate is 25 to 50 Hz.

The L2 trigger uses information from both the VD and DR. Preparing data for the L2 trigger takes approximately 50.0 μs. The L2 trigger rate varies from 10 to 20 Hz depending on the CESR running conditions. If a L2 trigger occurs, the CLEO II data acquistion system writes out all (or nearly all) detector data to disk. The overall trigger efficiency for $B\overline{B}$ events is 99.8%.

3.2.10 The Data Acquisition System

The purpose of the CLEO II data acquistion system [47] is to digitize the analog data from each detector element, in parallel, and write this information to disk. This can result in an enormous amount of data, since hundreds or even thousands of detector elements are used in each event. Using four Motorola 68040 microprocessors, the detector data are read into a temporary memory buffer in an average of 2 ms.

Fortunately, most events generated in e^+e^- collisions involve only a small number of particles, and therefore a small number of detector elements. To reduce the amount of unnecessary information, the detector signals are required to satisfy certain criteria to be considered further (e.g. the energy of a crystal in the CC must contain at least 2 MeV of energy). This sparcification process takes an additional 13 ms. The sparcified data are stored in another set of memory buffers, and built into a complete event. When the entire procedure is complete, the data are saved onto disk.

Data on disk is then analyzed with a software filter called Level 3 (L3). This filter was added to accommodate improvements in CESR luminosity, and allow looser trigger requirements for the study of rare and exotic B decays. Events passing L3 are written permanently to 4 mm tape.[8] End-user analysis can begin once the physical characteristics of these events (particle trajectories, shower positions, etc.) have been calculated.

[8] Along with a predetermined percentage of Bhabha and muon-pair events for offline calibrations.

Chapter 4

Event Reconstruction and Simulation

4.1 Introduction

After each detector element is read out by the data acquistion system, stored on disk, and filtered through L3, the data are finally saved onto magnetic tape. The format of the data on tape is not suitable for offline physics analysis, and must be converted. Before conversion, the data are stored in a "raw" format containing only digitized pulse heights and times. After conversion, the data are stored in a format containing physical quantities such as the momentum and energy of each particle. The converted, or compressed, data requires only 1% of the memory storage needed for raw data. Converting raw data into compressed data is called *event reconstruction.*

The reconstruction process is performed by a sophisticated software package called CLEVER. The CLEVER program uses a set of specialized processors which can interpret the raw data and write it into the compressed format. We then attempt to understand this output by comparing it to "artificial" data generated by a Monte Carlo simulation of the detector (see Section 4.5). In the following sections, a detailed description of the CLEVER processors are provided.

4.2 Track Reconstruction

We use the processors TRIO [48] and DUET [49] to identify and measure tracks left by charged particles in the tracking chambers. Track reconstruction with DUET is more efficient and accurate than TRIO, but takes considerably more computer time. For this reason, TRIO is used for online analysis, and DUET is used for offline analysis.

The transverse momentum (the momentum component perpendicular to the z axis) for each identified track, can be calculated from:

$$p_t = 0.3RB, \tag{4.1}$$

where p_t is the transverse momentum measured in GeV/c, R is the radius of the track in meters, and B is the strength of the magnetic field in Teslas. The total momentum of the track is then

$$p = p_t\sqrt{1 + cot^2\theta}, \tag{4.2}$$

where θ is the angle between the track and the beam line near the interaction point.

4.2.1 TRIO

The TRIO track-finding algorithm begins by identifying groups of three hits, from radially adjoining drift cells, throughout the tracking chambers. The criteria for combining hits differs in each tracking detector. In the PT, hits may come from any set of three adjacent layers. In the VD, hits must come from either the first five layers, or second five layers. In the DR, only hits belonging to the same axial layer are used.

TRIO then attempts to connect hit triplets from the innermost and outermost triplets in each detector. When combinations are found, TRIO fits a candidate track to the drift-time isochrones of the hits. Next, TRIO attempts to add new triplets to the candidate track. If new triplets are found, a new track is fit, and the process repeats itself. If at any point, the reconstructed track does not extrapolate closely to the interaction point, the track is abandoned. Typically, each cycle introduces four new triplets. When the process is complete, reconstructed tracks with good fit parameters are added to a permanent track list. This track list contains the momentum, direction, fit parameters, and vertex information for each track.

TRIO has difficulties finding triplets when dead or noisy wires are present. TRIO also has difficulty properly fitting low-momentum, tightly curling tracks. Such tracks are sometimes ignored, or fit to multiple tracks (one track for each spiral in the r-ϕ plane).

4.2.2 DUET

The DUET processor uses TRIO tracks as seeds for a more sophisticated track-finding procedure. In the DUET algorithm, track-finding begins by locating hit pairs in the r-ϕ plane. These hits are used to build a "hit tree". The longest, circular segments of each tree are taken as candidate tracks. These segments are defined further using z position information, and fit to a three-dimensional helix. As for TRIO, good tracks are stored in a permanent track list.

The momentum resolution can be divided into two pieces: (1) uncertainties in the individual position measurements due to the fit procedure, and (2) uncertainties due to multiple scattering. Theoretically, the momentum resolution depends on the momentum of the track, the uncertainty of each drift distance measurement, the strength of the magnetic field, and total length of the track fitted, the number of position measurements in the fit, and the thickness of the material in the path of the particle (usually given in radiation lengths). To calculate this theoretical resolution for the CLEO II tracking chambers, we assume an average of 49 r-ϕ track measurements, an average drift distance resolution of 150 μm, and an average material thickness of 0.025 radiation lengths. The resulting transverse momentum resolution is:

$$(\delta p_t/p_t)^2 = (0.0011 p_t)^2 + (0.0067)^2, \tag{4.3}$$

where p_t is the transverse momentum in GeV/c. The first term is due to uncertainties in drift distance measurements, and the second due to uncertainties in the track trajectory from multiple scattering.

The momentum resolution of the DUET processor is determined by a number of techniques [48]. Each technique relies on a source of clean, monoenergetic tracks in the data. At high energies, the resolution is determined using 5.29 GeV muons from $e^+e^- \rightarrow \mu^+\mu^-$ events. The measured momentum resolution using data (0.051 GeV/c) agrees well with the Monte Carlo simulation result (0.047 GeV/c).[1] The momentum resolution for muons in $e^+e \rightarrow \mu^+\mu^-$ events is shown in Figure 4.1. The angular resolution is $\delta\phi \approx 1$ mrad and $\delta\theta \approx 4$ mrad.

The simulation of the track-finding efficiency has also been checked carefully by a number of techniques [51] [52]. One such check involves a comparison of the ratio R=$\mathcal{B}(\eta^0 \rightarrow \pi^+\pi^-\pi^0)/\mathcal{B}(\eta^0 \rightarrow \gamma\gamma)$, where $\pi^0 \rightarrow \gamma\gamma$, in Monte Carlo and data.[2] Since there are two photons in each channel, the photon-finding efficiencies in this ratio cancel. The presence of two pions in the numerator allows us to check the track-finding efficiency. According to these studies, the Monte Carlo and data charged pion efficiency agree to within 2% (for momenta above 200 MeV/c).

[1] This agreement is reasonable since the Monte Carlo includes only the error in the transverse momentum. The error associated with the polar angle of each track is much smaller.

[2] The ratio R is measured to be approximately 0.61 [1].

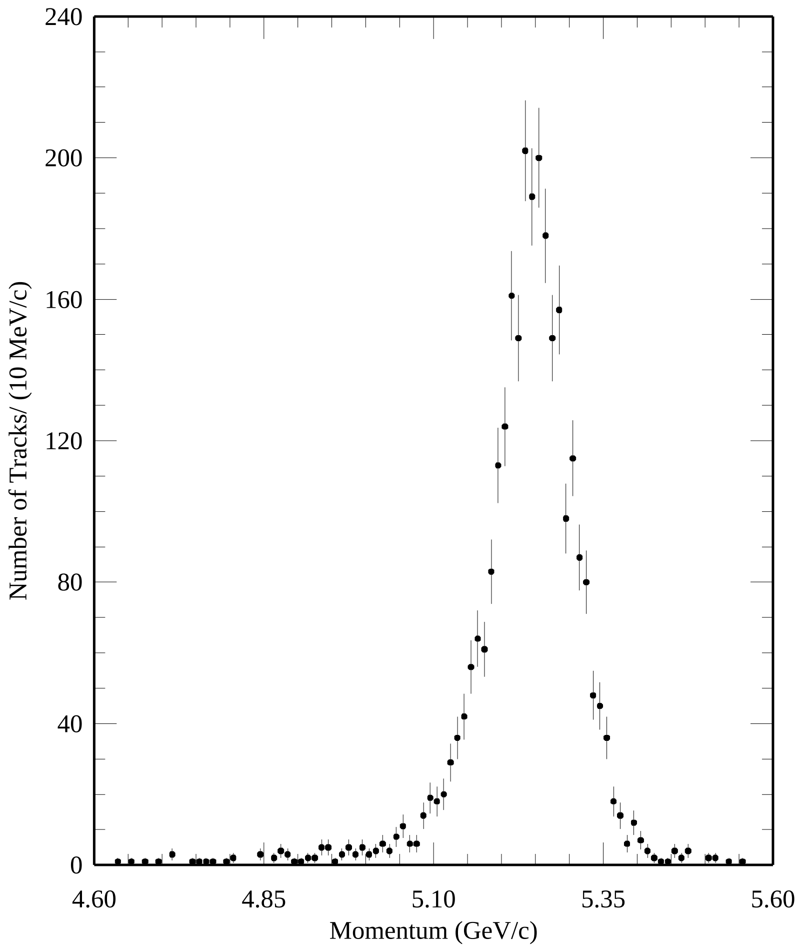

Figure 4.1: Measured muon momentum distribution for a sample of $e^+e^- \to \mu^+\mu^-$ events. (Courtesy of Jeff Nelson of the CLEO Collaboration.)

4.2.3 Rejection of Poorly Reconstructed Tracks

To eliminate poorly reconstructed tracks, we require all track candidates, except those from secondary decays such as $K^0_S \to \pi^+\pi^-$, to originate near the interaction point. Tracks identified as the inward-going half of a curler (see below) or without z information are discarded. To eliminate high-momentum tracks produced by incorrect fits, we discard tracks with measured momenta of 5 GeV/c or more.

4.2.4 Rejection of Curler and Ghost Tracks

The DUET algorithm occasionally fits more than one track to a set of hits. Extra tracks associated with these fits can be split into two categories: curler tracks and ghost tracks. Curler tracks occur when particles with a transverse momentum of less than $\approx$ 220 MeV/c and z momentum less than 45 MeV/c execute more than one spiral before leaving the tracking chambers. In this case, DUET fits multiple tracks to different sections of the spiral in the r-ϕ plane. Typically, this produces a pair of tracks: a primary arc corresponding to the particle's initial flight from the interaction region and a secondary arc corresponding to the return path. For each pair, the return track is rejected on the basis of ϕ separation ($\Delta\phi > 0.28\,$radians), the maximum transverse momentum ($P_t < 217\,$MeV/c), and the transverse momentum difference ($\Delta P_t < 80\,$MeV/c). If either track has a z momentum greater than 45 MeV/c, or if both tracks satisfy tight vertex requirements, the curler track hypothesis is abandoned. The tight vertex requirement is enforced by requiring the impact parameter with respect to the interaction point, `DBCD`, be less than 6.5 mm, the z position of the track at the interaction point, `ZOCD`, be less than 3.0 cm, and the residuals of the track fit (computed from the normalized sum of the differences between the measured and fit predictions of the drift distances), `RESICD`, be less than 0.45 mm.

Ghost tracks occur when two closely-spaced (i.e. nearly parallel) fits are associated with the same set of track hits. The recalcitrant track corresponds to the fit with the smallest number of z hits. A pair of tracks containing a ghost track is referred to as a “ghost pair”. Ghost pairs are identified on the basis of their ϕ separation ($\Delta\phi <$ .06 radians), momentum correlations ($\Delta P/P = 25\%$), and hit anti-correlations [55].

4.3 Shower Reconstruction

4.3.1 CCFC

As charged particles and photons pass into the calorimeter, they deposit energy into the crystals. The deposited energy appears as connected patterns of crystal hits in the calorimeter. Hits in the calorimeter may be produced by a single particle (e.g. charged pion), or by the overlap of multiple particles (e.g. merged photons from a π^0 decay).

The task of the CCFC processor is to reconstruct showers from crystal hits. Since the detection of electrons and photons take priority in most experimental applications, the reconstruction algorithm is optimized to identify and resolve electromagnetic showers.

The reconstruction process occurs in three steps: formation of connected regions, elaboration of connected regions into showers, and shower measurement. First, all crystals with an energy greater than 10 MeV/c are identified. These crystals are connected together if they are adjacent to one another. Then, the crystals in each connected region are ranked according to energy. The most energetic crystal is called a “primary seed”. The second most energetic crystal, that is not the nearest or next-nearest neighbor of the primary seed, is called the “secondary seed”. Additional seeds (if they exist) are defined in a similar manner.

To form a shower, each seed is connected with its nearest neighbors.[3] Next, the primary seed is associated with its next-nearest neighbors. Likewise, the secondary seed is associated with its next-nearest neighbors, provided that they are not yet claimed by

[3] In the barrel region of the CC, these groupings are straightforward; however, in the overlap and endcap regions the geometry is not as regular and groupings are somewhat larger.

the primary seed. If additional seeds exist, they are treated in the same fashion. This process continues until all nearby crystals containing deposited energy have been used. Often, crystal hits are left over after the shower reconstructed procedure. If such hits are nearest neighbors to a crystal in any shower, the hits are combined with the shower. Left over hits not assigned to a shower are discarded.

After the showers have been identified, their energies and positions are calculated. To reduce the effects of electronic noise, it is not optimal to use all crystals for the shower energy calculation. According to Monte Carlo calculations, the optimal number of crystals varies from 4 crystals for showers below 25 MeV to 17 crystals for showers above 4 GeV; a correction factor is applied to account for unused crystals. Additional corrections associated with lateral fluctuations in the showering process and leakage out the back of the crystals are also applied. The overall correction factor has been determined as a function of energy using radiative Bhabha events and isolated photons from π^0 decays. These correction factors have also been checked in the Monte Carlo.

The position of a shower is determined using the energy-weighted sum of the crystal centers. Correction factors are used to modify the predicted lateral position and depth of each shower. The lateral correction is related to the finite segmentation of the calorimenter, and is based on the position of the shower within the seed crystal. This correction is smallest at the crystal edges and center, and largest in between. The largest correction is approximately 1 cm. The average depth of a shower D is determined using Monte Carlo, and is given by:

$$D = 5.45 + 0.97 \ln E, \tag{4.4}$$

where E is measured in MeV and D is measured in cm. The exact depth of a given shower is between 8 and 15 cm. The shower energy and position resolutions for both the barrel and endcap regions are given in Table 4.1.

The simulation of the photon-finding efficiency has been checked using the ratio

Table 4.1: The energy and angular resolution of the CC. The energy is assumed to be measured in GeV, the angles are given in mrad.

Quantity	Barrel	Endcap
Energy	$\frac{\sigma_E}{E}[\%] = \frac{0.35}{E^{0.75}} + 1.9 - 0.1E$	$\frac{\sigma_E}{E}[\%] = \frac{0.36}{E} + 2.5$
ϕ	$\sigma_\phi = \frac{2.8}{\sqrt{E}} + 1.9$	$\sigma_\phi = \frac{3.7}{\sqrt{E}} + 7.3$
θ	$\sigma_\theta = 0.8\sigma_\phi \sin\theta$	$\sigma_\theta = \frac{1.4}{\sqrt{E}} + 5.6$

$R = \mathcal{B}(\eta^0 \to \pi^+\pi^-\pi^0)/\mathcal{B}(\eta^0 \to \pi^+\pi^-\gamma)$, where $\pi^0 \to \gamma\gamma$. Because there are two charged pions in each channel, the charged track efficiencies cancel. The presence of an additional photon in the numerator allows us to check the Monte Carlo prediction. According to this study, the Monte Carlo prediction for photon efficiency agrees with the true data efficiency to better than 2.5%.

4.3.2 Rejection of Showers Matched to Charged Tracks

Since neutral particles are identified by their showers in the CC, it is important to distinguish these showers from those created by charged particles. Fortunately, charged showers can be identified by their proximity to tracks in the DR.

The CDCC processor is responsible for determining if a shower is matched to a charged track. Two types of track-shower matches can occur: Type 1 and Type 2 [56]. A Type 1 match requires that the track pass within a certain distance of the shower. The geometry of a track-shower match, projected into the r-ϕ plane, is shown in Figure 4.2. Here, O is the interaction point, C is the center of the track helix, and S is the center of the shower. As mentioned in the previous section, the exact depth of the shower is a function of energy; however, for matching purposes the depth is defined to be 15 cm (half the length of the crystal). The distance of closest approach is expressed in terms

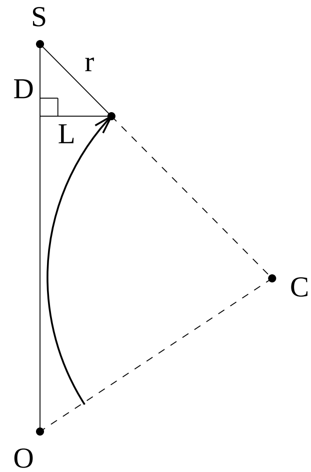

Figure 4.2: A schematic of the track-shower matching projection method. A Type 1 match requires that L be less than 8 cm, and D be less than 15 cm. (The distance of closest approach for a particle produced at the origin 0 is typically less than 0.1 cm.)

of a radial (D) and lateral (L) component. A Type 1 match requires that L be less than 8 cm, and D be less than 15 cm. Similarly, a Type 2 match requires that the track pass within a certain distance of a crystal center within a shower. These criteria were optimized using electron and photon showers in the data.

4.3.3 Rejection of Merged Showers and Shadow Showers

Complications in track-shower matching arise for two types of showers: merged showers and shadow showers. A merged shower occurs when multiple particles are associated with a single shower; that is, when the electromagnetic cascade of two or more individual particles overlap. Merged showers may or may not result in a mismeasurement of the total neutral energy. For example, a merged shower produced by a charged and neutral particle may result in the unwanted removal of neutral shower energy through track-shower matching. According to Monte Carlo studies, this situation occurs rarely. Conversely, a merged shower created by two closely-spaced photons from $\pi^0 \to \gamma\gamma$ decay does not adversely affect the measured event energy since total energy of the photons is recorded.

In contrast to a merged shower, a shadow shower occurs when multiple showers are associated with a single particle. For example, nuclear material produced by a hadronic interaction in the calorimeter may travel an appreciable distance before creating another separate shower (or "hadronic splitoff"). Such showers are unwanted since they lead to an overestimate of the total neutral energy since they are not identified in track-shower matching. Fortunately, shadow showers may be identified by their proximity to showers matched to a charged track. In particular, we require the angle between each shadow shower candidate and the nearest matched shower to be separated by less than $9°$ in θ and less than $10°$ in ϕ. We further require that the shower energy distribution for each shadow shower candidate (see Section 4.4.4) not be consistent with a photon. These criteria were optimized using hadronic showers in the data [57].

4.3.4 Rejection of Showers With Malfunctioning Crystals

Electronic noise associated with individual crystals can degrade the energy resolution of showers. Showers containing, or near to, crystals known to be have electronic noise for a given run are rejected. To eliminate the effects of "noisy" crystals in shower reconstruction, we impose a minimum shower energy requirement of 30 MeV.

4.4 Particle Identification Techniques

The identification of particles is essential to a complete understanding of each event. In this section, we describe several techniques for identifying the charged particles: electrons, muons, pions, kaons, and protons. These techniques exploit the different ways that each particle type interacts with the detector. At the end of the section, a scheme for resolving the identity of particles consistent with more than one particle hypotheses is given.

4.4.1 Ionization Energy Loss (DR)

The amount of specific ionization energy loss, dE/dx, a charged particle experiences as it passes through the tracking chambers can be related directly to the particle's velocity. According to the well-known Bethe-Bloch formula, the average dE/dx loss varies as $1/\beta^2$ at non-relativistic velocities, and after passing through a minimum at $E \approx 3Mc^2$, increases logarithmically with $\gamma = (1-\beta^2)^{-1/2}$. Furthermore, this loss is independent of the mass of the traversing particle. Hence, at a given momentum, heavier slower-moving particles will experience a larger ionization loss. In this thesis, ionization energy loss is used primarily for hadron identification.

The dE/dx loss at each sense wire is determined by dividing the measured charge by the path-length through the drift cell. The dE/dx loss of each particle is defined as the mean of the dE/dx measurements over the length of each track. These measurements use 39 layers of axial sense wires, and 11 layers of stereo sense wires. The dE/dx measurement of a typical track in the barrel is based on approximately 30 good hits. For each track, the dE/dx measurements are expected to be approximately equal, since the ionization energy loss is negligible ($\approx$ 5.0 KeV/cm) on the momenta of high-energy particles ($p > 100$ MeV/c).

Due to occasional "close" primary collisions, the dE/dx distribution contains a high-energy Landau-like tail. While such collisions are infrequent, they produce a large effect on the mean of the dE/dx distribution. To reduce this effect, dE/dx measurements above the median for each track are discarded. This procedure improves the estimation of the average dE/dx loss [59].

The DEDR processor takes the raw data at each sense wire, and corrects it for the two additional effects:

a) Dip angle saturation. Saturation occurs when ions, released by the passage of a track, electrically shield other electrons from the sense wire. This effect reduces the collected charge at the wire. The magnitude of this effect depends on the polar angle of track, and is largest for angles near 90°.

b) Drift distance. The total charge collected at a wire depends on the distance the electrons travel from the track to the wire. As mentioned in Section 4.2, the precise path of travel can be complicated by magnetic field effects. The drift distance is also known to be affected by the entrance angle of the track into the drift cell, the charge of the particle, and the specific axial-stereo layer used.

The gas mixture, gas temperature, and atmospheric pressure can also affect the amount of ionization created in each drift cell. Further, the effect of broken field wires in nearby cells, and differences in wire-to-wire electronic gains may also affect the ionization loss measurement. To account for these effects, corrections based on studies of Bhabha events are applied.

After accounting for the above dependencies, a final value for dE/dx for a given track can be determined. For a track with 40 or more good hits, a dE/dx resolution of 6.2% is achieved for Bhabha electrons, and a resolution of 7.1% for minimum-ionizing pions. The separation of particle types achieved by this method is shown in Figure 4.3.

Next, the DEDR processor compares the measured dE/dx values with the expected values. The difference between these values is expressed in terms of the standard deviation of the dE/dx measurement. For example, the difference between the measured and expected dE/dx loss for a pion (`SGPIDI`) is defined by:

$$\texttt{SGPIDI} \equiv \left(\frac{(\frac{dE}{dx})_{\text{meas}} - (\frac{dE}{dx})_{\text{exptd}}}{\omega} \right)_{\pi}, \tag{4.5}$$

where ω is the measured width of the pion dE/dx distribution. The corresponding quantities for kaons and protons are referred to as `SGKADI` and `SGPRDI`, respectively.

4.4.2 Direct Velocity Measurement (TOF)

The TFAN processor takes the raw TOF data and calculates, with corrections, the travel time of a particle passing from the interaction point to the TOF counters. The

Figure 4.3: dE/dx as a function of momentum. Theoretical predictions for various types of particles are indicated by curves on the plot.

TOF measurement, together with an estimate of the path length of the track, can be used to calculate the velocity (β) of the particle. As mentioned in the previous section, the measured velocity of a particle may be used for particle identification. The separation of particle types achieved by this method is shown in Figure 4.4. Like dE/dx measurements, the difference between the measured and expected TOF measurements is expressed in terms of the standard deviations of these measurements.

4.4.3 Energy-Momentum Ratio (DR and CC)

This technique is used to identify electrons. Since electrons deposit nearly all of their energy in the crystals, the energy of an electron shower is approximately equal to the momentum of the matched track (the electron mass is negligible). Other particles, such as muons and pions, deposit only a small fraction of their energy into the crystals (see Section 3.2.6). Hence, the ratio of energy to momentum (E/p) for electrons is approximately 1.0, and for other particles is typically much less than 1.0. A comparison of E/p for electrons and hadrons in given in Figure 4.5.

4.4.4 Shower Shape (CC)

As mentioned in the previous section, electrons and photons lose a large fraction of their energy in the calorimeter. The process responsible for this loss occurs very rapidly, producing a very well-confined shower. In contrast, charged or neutral hadrons that interact hadronically with the calorimeter deposit energy in a more diffuse pattern. To discriminate between electromagnetic showers and hadronic showers, we use the shower-shape quantity, E_9/E_{25}, where the variable E_9 is the energy of the all crystals out to nearest neighbors of the primary seed, and E_{25} is the energy of all crystals out to its next-nearest neighbors of the primary seed. Consequently, E_9/E_{25} is large for electrons and photon showers, and smaller for hadronic showers (see Figure 4.6).

Figure 4.4: Measured time of flight as a function of momentum. Predictions for various types of particles are indicated by lines on the plot.

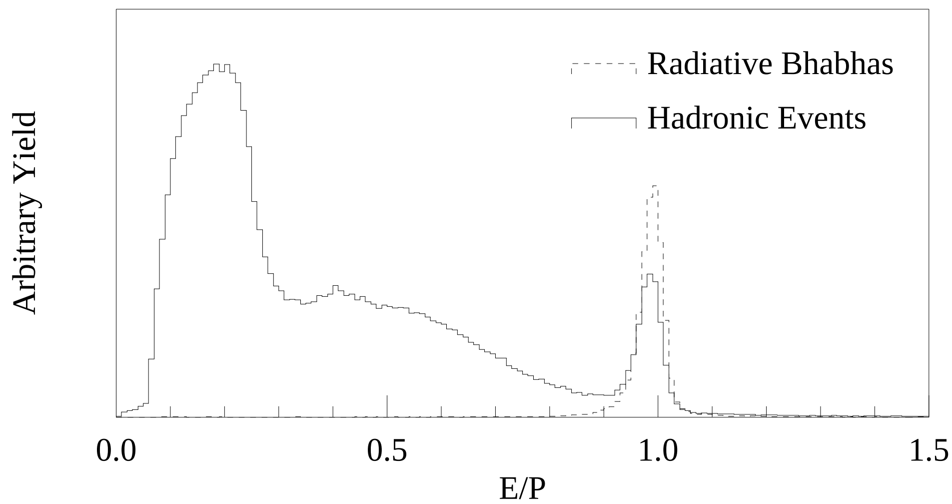

Figure 4.5: The ratio of shower energy to track momentum (E/p) for electrons from radiative Bhabha events (dotted line) and hadronic events (solid line). For each track candidate, we require $0.8\ \mathrm{GeV/c} < p_\ell < 3.0\ \mathrm{GeV/c}$, and that the particle deposit energy in the barrel calorimeter. (Courtesy of Steve Schrenk of the CLEO Collaboration.)

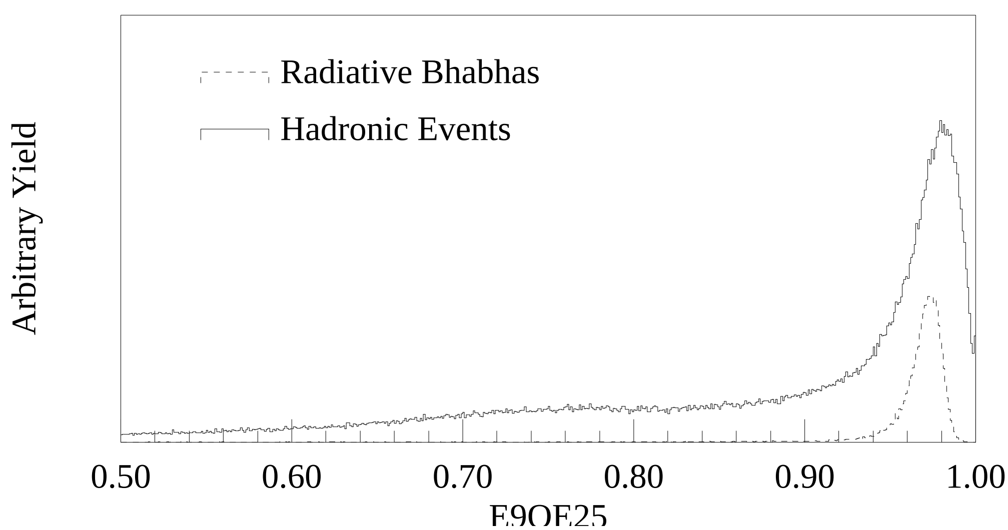

Figure 4.6: The ratio of the energy in the 9 innermost crystals and the 25 innermost crystals (E_9/E_{25}). The ratio is approximately 1.0 for electrons and photons, and frequently less for other particles. For each track candidate, we require $0.8\ \mathrm{GeV/c} < p_\ell < 3.0\ \mathrm{GeV/c}$, and that the particle deposit energy in the barrel calorimeter. (Courtesy of Steve Schrenk of the CLEO Collaboration.)

4.4.5 Muon and Tracking Chamber Hits (DR and MU)

Muon and tracking chamber hits can be used to identify muons. Muon identification relies on the ability of muons to penetrate the plastic TOF scintillators, the cesium-iodide crystals, the magnetic coil, several inches of iron, and finally, registered hits in the muon chambers.

The MUTR processor uses the muon hypothesis to project each drift chamber track through the inner detector components, and into the muon chambers. This projection takes into account multiple scattering, ionization energy loss, and magnetic field effects. To be identified as a muon, candidate tracks must have hits in all of the super layers where hits have been predicted. In addition, the identified muon must also have at least two hits in the outermost superlayer it is predicted to reach. The penetration depth of identified muons is calculated in nuclear absorbtion lengths.[4]

4.4.6 Particle Identification Requirements

The objective of a particle identification scheme is to combine all the identification techniques above to resolve the identity of each particle in an event. Below we describe specific consistency cuts for each particle type, and then describe the scheme to resolve conflicts where a particle is consistent with more than one identification hypothesis.

Specific Consistency Cuts

a) Hadrons ($\pi^{\pm}$, $K^{\pm}$, p, and $\bar{p}$). Hadron identification is based solely on ionization energy loss measurements in the DR. In particular, the observed dE/dx loss of the hadron candidate must be consistent with the predicted loss within 2.0 sigma. For example, an identified pion must have $|\texttt{SGPIDI}| < 2.0$.

---

[4] One nuclear absorbtion length is the mean free distance over which a strongly-interacting particle will collide inelastically with a nucleus (only 16.7 cm in iron).

b) Muons ($\mu^{\pm}$). Muon identification is based solely on muon and track chamber hit information. Each candidate muon track is assigned the depth of the outermost unit in which at least two of three layers in the superlayer are hit. The quantity, `DPTHMU`, is defined as the maximal depth reached by the muon candidate in nuclear absorbtion lengths. To identify muons we require `DPTHMU` > 3. If, according to track extrapolation, there are other units at depths greater than the maximal reached that are expected to have hits but have no hits (i.e. if the track's depth is less than predicted), then the muon hypothesis is rejected.

The muon detection efficiency is degraded by material effects, geometric acceptance, and chamber efficiency. The efficiency to detect low momentum muons is also limited since these particles may curl within the tracking chambers without reaching the MU detector. The momentum threshold to enter the outermost muon detectors is approximately 1.8-2.0 GeV, depending on the polar angle of the track. The geometric and chamber efficiency for muons is determined with a high statistics sample of $e^{+}e \rightarrow \mu^{+}\mu^{-}$ events, and used as input to the Monte Carlo. The Monte Carlo and data muon efficiency in the threshold region agree to within 0.5% [60]. This agreement reflects a good understanding of the amount of material in front of the muon chambers.

The muon fake rate, or the probability that hadrons are misidentified as muons, is contributed by four sources: random matches, decays in flight, "punch through" hadrons, and "sail through" hadrons. A random match occurs when a set of noise or cosmic-ray hits in the muon chambers is inadvertantly matched with a track in the drift chamber. These matches occur very rarely since the muon identification scheme requires a minimum of six matched wires or strips for a muon to be detected. Decays in flight, such as $K \rightarrow \mu\nu$ and $\pi \rightarrow \mu\nu$, produce real muons which enter the muon counters. A "punch through" hadron is a hadron that interacts via the strong interaction, usually with the muon iron, producing secondary particles that reach the muon counters. A "sail through" hadron is a hadron that passes through the iron and into the muon counters.

The muon fake rate is determined by several techniques. A summary of these techniques is given in Reference [61]. Each technique relies on a source of nearly pure hadrons. One means to obtain a hadron sample is by tagging hadrons in well-known decay processses such as $\overline{D}^0 \to K^{\pm}\pi^{\pm}$ or $\tau \to \overline{\nu}_\tau h\pi^0$ in which the recoiling τ decays leptonically. It is also possible to obtain a nearly pure hadron sample from Υ(1S) data. In this case, a small source of leptons from the process $\Upsilon(1S) \to \gamma^* \to q\overline{q}$, together with the continuum contribution, must be subtracted using off-resonance Υ(4S) data. According to these studies, the muon fake rates for `DPTHMU` > 3, 5, and 7, corresponding to momenta above 1.0, 1.5, and 2.0 GeV/c, are approximately constant at 3.5%, 1.4%, and 0.8% (for good barrel muons only).

c) Electrons ($e^{\pm}$). Electron identification is based primarily on dE/dx and E/p measurments. To a lesser extent, the following quantities are also used: E_9/E_{25}, TOF measurements (in the barrel region), the ratio of shower width in the θ and ϕ directions, and the track-shower match distance. This information may be combined into a log-likelihood (`R2ELEC`) of a particle being an electron. This log-likelihood is defined by:

$$\texttt{R2ELEC} = \sum_{variables} \ln \frac{\mathcal{P}_e}{\mathcal{P}_{\neq e}}, \tag{4.6}$$

where $\mathcal{P}_e$ is the joint probability that an electron will produce a track with the values measured, and $\mathcal{P}_{\neq e}$ is the joint probability that a non-electron will produce the same values. If an identification measurement for a candidate track is unavailable, the corresponding terms in the likelihood variable are dropped. This technique allows us to identify electrons down to 400 MeV.

To identify electrons, we require `R2ELEC` > 3.0 in the barrel region of the calorimeter, and `R2ELEC` > 1.0 in the bad barrel, overlap, and good end cap regions (see Section 3.2.6). The $\mathcal{P}_e$ distribution is determined by embedding hits from electron tracks from radiative Bhabha events into hadronic events. The $\mathcal{P}_{\neq e}$ distribution is determined using

$\Upsilon(1S)$ data. Values of R2ELEC in the Monte Carlo are simulated using the $\mathcal{P}_e$ and $\mathcal{P}_{\neq e}$ distributions above.

The electron efficiency is determined by embedding electrons from radiative Bhabha events in hadronic events. For the requirement R2ELEC > 3.0 this efficiency rises from 90% to 95% with increasing momentum [62]. The assumption that embedded electron events look like real events introduces a systematic uncertainty of approximately 5% on the electron identification efficiency [63].

The electron fake rate is estimated using many of the same techniques used to determine the muon fake rate [64]. The pion fake rate for electrons varys roughly from 0.1% below 1 GeV/c to 0.4% at 3 GeV/c. The kaon and proton fake rates are not well-known due to a lack of statistics.

A Particle Identification Scheme

Often, the identity of a candidate track is consistent with multiple particle hypotheses. To resolve these conflicts, we first assume that all tracks are pions. This is a good approximation for $B\overline{B}$ events, where approximately 8 in every 10 tracks is a pion. If the track is also consistent with the electron or muon hypothesis, the identity of the track is analyzed further. If the track is consistent with the electron hypothesis, but not the muon hypothesis (see the definitions above), we assign the electron mass to the track; if not, we assign the muon mass to the track.

If a track is not an electron or muon, but is consistent with the kaon hypothesis, we assign the kaon mass to the track. If the track is not an electron, muon, or kaon, but is consistent with the proton hypothesis, we assign the proton mass to the track. This scheme improves the total charged energy resolution, with respect to the simple pion-mass hypothesis, by approximately 15%.

4.5 Monte Carlo Simulation

Since the CLEO II detector is a complicated device, we need to use a Monte Carlo simulation to understand how our detector will respond to various decay processes. The term “Monte Carlo” is connected to the use of random number generators to model inherently random physical phenomenon such as decay processes.

To produce Monte Carlo events, a user must first provide a set of data files that describe a desired decay process, or list of decay processes, that follow from a hypothetical e^+e^- annihilation. This data specifies the decay probability and dynamics of all particles in each event. In some cases, decay processes not explicitly provided by the user (perhaps from secondary and tertiary decays) are provided by a comprehensive default data file which summarizes our knowledge of particle physics.

The above data are then fed into a routine which randomly determines the momentum and energy of all specified particles according to the kinematics and dynamics of each decay. A detector simulation routine called `CLEOG` [65] propagates these particles through a model of the CLEO II detector. This routine is capable of modeling hadronic interactions, electromagnetic showers, multiple scattering, photon conversions, ionization, and many other physical processes in the detector.

Ultimately, the destiny of each particle is determined by random number generators. `CLEOG` may indicate, for example, that a particle is lost in a spontaneous decay process in the DR, or absorbed in the MU system. After all particles have been propagated, `CLEOG` calculates the estimated response of the detector in terms of pulse heights and times, and writes the event out in raw format. The raw data are then converted into a compressed format using the same processors used for the data events.

Monte Carlo simulations are used extensively to study the detector performance and analysis software. For example, in Chapter 7, we study the response of the CLEO II detector to $B \to \ell\overline{\nu}_\ell\gamma$ decays. Several thousand Monte Carlo events are used to determine the efficiency of detecting the lepton and photon in each event. In addition, millions of potential background events are also simulated. The total number of lepton-photon pairs in this sample, consistent with a $B \to \ell\overline{\nu}_\ell\gamma$ hypothesis, are used to determine the predicted background level. Having tested that the Monte Carlo does an adequate job of modeling signal and background events, these results can be used to predict the overall sensitivity of the CLEO II detector to $B \to \ell\overline{\nu}_\ell\gamma$ decays.

4.6 A Reconstructed CLEO II Event

An example of a reconstructed CLEO II event is shown in Figure 4.7. In this view, the positive z axis is out of the page. The center of the figure represents the tracking chambers. Individual drift chamber hits and the reconstructed tracks are superimposed. The thin ring just outside the tracking system corresponds to the TOF system, and the thick circular grid outside the TOF system corresponds to the CC. The barrel of the calorimeter is rendered in a single-point perspective; in this view, the outer regions of the grid are closer to the viewer, and the inner regions are farther away. Hits within the CC are represented by closed rectangles. The reconstructed shower energies are given in GeV. The open squares at the center of the figure represent hits in the endcap calorimeter. The muon system is represented by the outer octagonal region. In this region, the closed circles represent hits on the anode wires, and the long black bars represent hits in the cathode strips.

The data event shown in the Figure 4.7 is a candidate event for the process $e^+e^-\to\tau^+\tau^-$ where the τ^+ decays to $\mu^+\nu_\mu\overline{\nu}_\tau$ and the τ^- decays to $\pi^+\pi^-\pi^-\nu_\tau$. Track 1 corresponds to the muon candidate, since it is matched to a series of hits in the muon chambers. According to dE/dx information, tracks 2,3 and 4 are consistent with being pions. All charged tracks are matched to showers in the calorimeter. According to the shower reconstruction, track 3 is matched to two showers, with energies 740 MeV and 180 MeV. The 20 MeV shower neighboring the 420 MeV shower (matched to track 4) is

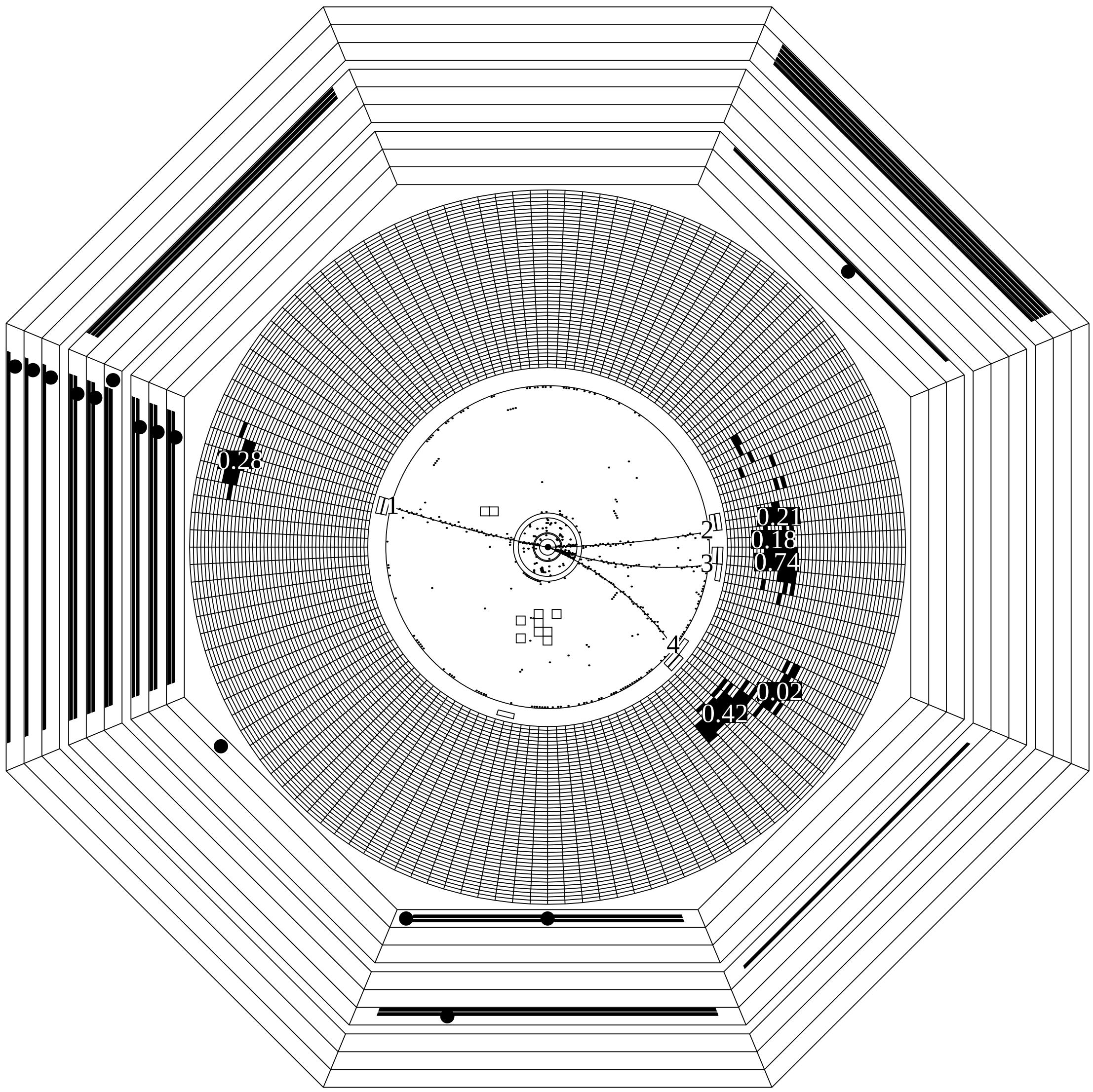

Figure 4.7: An example of a reconstructed CLEO II event. (Courtesy of Jeff Nelson of the CLEO Collaboration.)

interpreted as a shadow shower. The neutrinos in this event are undetected.

Chapter 5

A Search for $B \to \mu\bar{\nu}_\mu$ and $B \to e\bar{\nu}_e$ Decays

5.1 Signal Decay Kinematics

In $B \to \mu\overline{\nu}_\mu$ and $B \to e\overline{\nu}_e$ decays, the lepton and neutrino are produced back-to-back with approximately equal momentum. Since both the muon and electron mass are small relative to the B meson mass, the decay kinematics for $B \to \mu\overline{\nu}_\mu$ and $B \to e\overline{\nu}_e$ are essentially identical. In B rest frame, the lepton momentum for these decays is constrained to be approximately $m_B/2$, where m_B is the B meson mass. In the lab frame the observed lepton momentum distribution is Doppler broadened by $\pm 6\%$ due to the motion of the parent B (see Section 3.1.3).

A number of other important kinematic features of $B \to \ell\overline{\nu}_\ell$ decays may also be identified. Consider a $B\overline{B}$ event in which the first B ($B1$) decays to $B \to \ell\overline{\nu}_\ell$, and the second B ($B2$) decays generically (i.e. randomly, through other decay processes). Assuming the neutrino in the $B \to \ell\overline{\nu}_\ell$ decay is the only undetected particle in the event, the total energy of the remaining particles should be consistent with the energy of a single B. This constraint is expressed by:

$$E_{B2} \equiv \sum_i \mathrm{E}_i = \mathrm{E}_{\mathrm{beam}} = 5.29 \text{ GeV}, \tag{5.1}$$

where E_i is the energy of the i-th particle from the second B. The sum energy of the particles from the second B equals the beam energy since B mesons are produced in an e^+e^-collision. Given the energy of the second B and the known B mass, the momentum of the second B, $p_{_{B2}}$, can be determined. Values of $p_{_{B2}}$ are therefore constrained by:

$$M_{B2} \equiv \sqrt{\mathrm{E}_{\mathrm{beam}}{}^2 - p_{_{B2}}{}^2} = m_{_B} = 5.28 \text{ GeV}, \tag{5.2}$$

where M_{B2} is referred to as the "beam-constrained mass" [66].

Having dealt with quantities that characterize the second B, we require that the missing energy, E_ν, and missing momentum, P_ν, of the event be consistent with the presence of a massless neutrino; that is, we require $E_\nu = P_\nu$. This condition may be transformed into a requirement on the lepton momentum. Since $\vec{p}_{_{B1}} = -\vec{p}_{_{B2}}$ and $p_{_{B1}} \ll p_{_\ell}$, the neutrino mass constraint implies:

$$\mathrm{E}_{\mathrm{beam}} - E_{_\ell} = |\vec{p}_{_{B1}} - \vec{p}_{_\ell}|, \quad \text{and} \tag{5.3}$$

$$\mathrm{E}_{\mathrm{beam}} - p_{_\ell} \approx p_{_\ell} - p_{_{B1}} \cos\theta_{\ell \cdot B2}, \tag{5.4}$$

which reduces to:

$$p_\ell^* \equiv p_\ell + \frac{p_{B2}}{2} \cos\theta_{\ell \cdot B2} \approx \frac{m_{_B}}{2}, \tag{5.5}$$

where p_ℓ^* is the "corrected" lepton momentum, or the lepton momentum in the B rest frame. This quantity is composed of two terms: (1) the observed lepton momentum, and (2) a correction to the lepton momentum due to the motion of the parent B.

5.2 Event Selection

5.2.1 General Method

Guided by the above kinematic constraints, we search for $B \to \ell\overline{\nu}_\ell$ decays in $B\overline{B}$ events created at $\Upsilon(4S)$ resonance by requiring a lepton with a momentum of approximately $m_B/2 = 2.64$ GeV, and the sum energy and beam-constrained mass (or momentum) of remaining particles to be consistent with the decay of a second B.

5.2.2 The Data Sample

The data sample used in this measurement consist of approximately 2.7 million $\Upsilon(4S) \to B\bar{B}$ events and 9.9 million continuum events collected at $\sqrt{s} = 10.58$ GeV (the "on-resonance" sample). Of the continuum sample, approximately 86% are $e^+e^- \to q\bar{q}$ events. We also use a sample of 5.1 million continuum events collected below resonance at $\sqrt{s} = 10.52$ GeV for background subtraction (the "off-resonance" sample). The on- and off-resonance samples correspond to an integrated luminosity of 2.5 fb^{-1} and 1.3 fb^{-1}, respectively. The use of the off-resonance sample is described in detail in Section 5.3.1.

5.2.3 Selecting Hadronic Decays

To search for $B \to \ell\overline{\nu}_\ell$ decays, we first select hadronic candidates based on the event-vertex position. The event-vertex position is defined as the point closest to the largest number of tracks, and must be within 2 cm of the interaction point in r-ϕ plane, and with 5 cm in the z direction. This requirement rejects beam-wall, beam-gas, and other junk events. We also require at least 3 tracks in the DR (tracks from K^0_S and photon conversions count as 1 track). The total event energy must be greater than 15% of the center-of-mass energy. The efficiency of hadronic event selection cuts on Monte Carlo $B\overline{B}$ events is approximately 99%. These cuts rejects QED events such as Bhabha and muon-pair events [67].

5.2.4 Selecting Signal Decays

Once a suitable sample of hadronic events has been selected, we search for events containing a lepton with a momentum of approximately 2.64 GeV. For each lepton candidate, we attempt to identify and measure all particles attributed to the second B. A detailed description of this procedure is given below.

The Lepton

To identify the lepton in a $B \to \ell \overline{\nu}_\ell$ decay, we begin by identifying *all* leptons in each event in the hadronic sample. Electrons with momenta above 1.8 GeV are identified by their electromagnetic interactions in the calorimeter, their ionization-energy loss in the drift chamber gas, and their velocities measured in the time-of-flight system. In particular, we require `R2ELEC` > 3 (see Section 4.4.6). Electrons within the geometrical acceptance ($|\cos\theta_e| < 0.85$) are identified with an efficiency of approximately 94%. Muons are identified by their ability to penetrate through at least 7 nuclear absorption lengths of crystal and iron and produce hits in the muon tracking chambers; specifically, we require `DPTHMU` > 7. This requirement puts a lower limit of approximately 2.0 GeV on the muon momentum acceptance. Muons within the geometrical acceptance ($|\cos\theta_\mu| < 0.85$) are identified with an efficiency of approximately 85%.

Each lepton candidate must also fulfill strict vertex requirements. In particular, we require the impact parameter with respect to the interaction point, `DBCD`, be less than 1.5 mm, the z position of the track with respect to the interaction point, `ZOCD`, be less than 3.5 cm. We also require the candidate tracks to have good z information, and not be identified as the inward-going half of a curler. One lepton candidate per event is chosen based on the highest momentum lepton in the event. According to the Monte Carlo, if the signal lepton falls within the detector acceptance and passes the above